CHALMERS
UNIVERSITY OF TECHNOLOGY

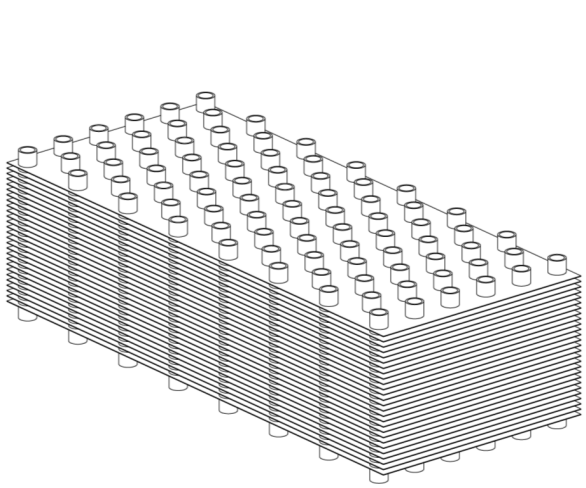

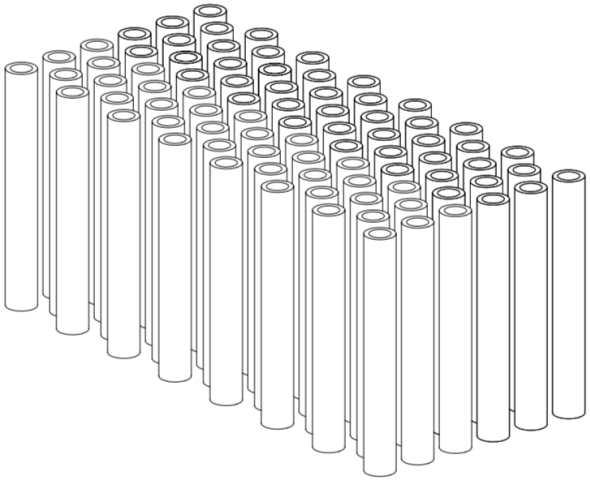

Development of a Validated CFD Model For Simulation of Tube Heat Exchangers

A Comparison of Methods and Models

Master's thesis in Mobility Engineering

Vincent Fröberg

Axel Johansson

DEPARTMENT OF MECHANICS AND MARITIME SCIENCES

CHALMERS UNIVERSITY OF TECHNOLOGY
Gothenburg, Sweden 2026
www.chalmers.se

Master's thesis 2026

Development of a Validated CFD Model For Simulation of Tube Heat Exchangers

A Comparison of Methods and Models

VINCENT FRÖBERG
AXEL JOHANSSON

CHALMERS
UNIVERSITY OF TECHNOLOGY

Department of Mechanics and Maritime Sciences
Division of Fluid Dynamics
Chalmers University of Technology
Gothenburg, Sweden 2026

Development of a Validated CFD Model For Simulation of Tube Heat Exchangers
A Comparison of Methods and Models
VINCENT FRÖBERG
AXEL JOHANSSON

Supervisor: Petter Miltén, Department of Mechanics and Maritime Sciences
Examiner: Carlos Xisto, Department of Mechanics and Maritime Sciences

Master's Thesis 2026
Department of Mechanics and Maritime Sciences
Division of Fluid Dynamics
Chalmers University of Technology
SE-412 96 Gothenburg
Telephone +46 31 772 1000

Cover: 3D visualizations of the two analysed heat exchangers. Not to scale.

Typeset in LaTeX
Printed by Chalmers Reproservice
Gothenburg, Sweden 2026

Development of a Validated CFD Model For Simulation of Tube Heat Exchangers
A Comparison of Methods and Models
VINCENT FRÖBERG
AXEL JOHANSSON
Department of Mechanics and Maritime Sciences
Chalmers University of Technology

Abstract

Thermal management is an increasingly relevant topic within a range of engineering fields and industries. From cooling of batteries in electric cars and trucks to higher efficiency turbofan engines, the demand for well performing and lightweight compact heat exchanger designs is high. Having the ability to measure the performance of a heat exchanger geometry using numerical methods with good confidence in the results is of great benefit as it can save time and money compared to experimental methods. In this thesis, two tube heat exchanger geometries have been modelled and simulated in Siemens Star-CCM+, a commercial CFD software. The heat exchanger geometries are taken from the book *Compact Heat Exchangers* (1984) by William M. Kays and Alexander L. London. This book contains experimental data for a wide range of heat exchanger designs. The simulation models are validated by comparing two key performance parameters for heat exchangers to experimental data; the Fanning friction factor and the Colburn j-factor. Two modelling approaches have been investigated; a ”single channel” approach and a ”unit cell” approach. Using a ”single channel” approach with a steady coupled solver, friction factor values within 5% error to experimental values are achieved across most Reynolds numbers for both heat exchangers. Colburn j-factor values within 10-12% error to experimental values are achieved for the tube heat exchanger and within 23-28% for the finned tube heat exchanger. Results show that the SST k-omega turbulence model together with the Gamma-ReTheta transition model show the best ability to match experimental results and trends for both geometries.

Keywords: CFD, heat exchanger, thermal management, Star-CCM+, computational fluid dynamics, heat transfer, turbulence models

Acknowledgements

We would like to thank our examiner Carlos Xisto and our supervisor Petter Miltén for their support and guidance throughout this master thesis. We also want to thank Isak Jonsson for his time and input.

Vincent Fröberg & Axel Johansson, Gothenburg, June 2026

List of Acronyms

Below is the list of acronyms that have been used throughout this thesis listed in alphabetical order:

BC	Boundary Condition
CFD	Computational Fluid Dynamics
DNS	Direct Numerical Simulation
EB	Elliptic Blending
FVM	Finite Volume Method
HEX	Heat Exchanger
LES	Large Eddy Simulation
RANS	Reynolds Averaged Navier Stokes
SST	Shear Stress Transport
TKE	Turbulent Kinetic Energy
URANS	Unsteady RANS

Nomenclature

Below is the nomenclature for the main symbols that has been used throughout this thesis.

Symbols

A	Total heat transfer area
A_c	Minimum free-flow area
A_f	Fin surface area
c_p	Specific heat at constant pressure
D_h	Hydraulic diameter ($D_h = 4A_cL/A$)
D_t	Tube diameter
f	Fanning friction factor
G	Mass velocity ($\dot{m}/A_c$)
H	Height of domain
h	Heat Transfer Coefficient
h_{ideal}	Corrected "ideal" heat transfer coefficient for the fin-tube geometry
j_H	Colburn j-factor
K_c	Contraction loss coefficient for flow at heat exchanger entrance
K_e	Expansion loss coefficient for flow at heat exchanger exit
k	Thermal conductivity
L	Heat exchanger flow length (characteristic length)
L_f	Effective fin length
$\dot{m}$	Mass flow rate
n	Number of full tube rows
P_0	Total Pressure
p_f	Fin pitch
p_l	Longitudinal tube pitch

p_t	Transverse tube pitch
Q	Heat transfer
T	Temperature
T_{in}	Temperature at the inlet of the domain
T_m	Mean temperature (mean of T_{in} and T_{out})
T_{out}	Temperature at the outlet of the domain
T_w	Wall temperature
t_f	Fin thickness
V	Free-stream velocity of the fluid
v	Specific volume
W	Width of channel
ΔT_{lm}	Logarithmic mean temperature difference
η_f	Fin efficiency
η_o	Overall surface efficiency
ν	Kinematic viscosity
μ	Dynamic viscosity
ρ	Density
ρ_m	Mean density

Contents

List of Figures

List of Tables

1
Introduction

1.1 Background

Thermal management is an increasingly relevant topic within a range of engineering fields and industries due to the continuous increase in energy efficiency requirements across a broad range of industries. From cooling of batteries in electric cars and trucks to higher efficiency turbofan engines, the demand for well performing and lightweight compact heat exchanger designs is high. Novel heat exchanger designs such as gyroid structures require more complex and expensive manufacturing methods such as metal additive manufacturing. Having the ability to measure the performance of a heat exchanger geometry using numerical methods with good confidence in the results is of great benefit as it can save time and money compared to experimental methods. Modelling heat exchangers is not as simple as it may seem however. Performance values range with decimals in the hundredths or thousandths, and require thus high numerical precision to be captured correctly. Therefore, even small inaccuracies in the physical and numerical setup can render significant deviations in the simulation results. Furthermore, flow in heat exchangers contain transitional and turbulent flows that need to be modelled instead of solved directly. Computational Fluid Dynamics (CFD) has made significant advancements in the past decades, with improved algorithms and increased accessibility in academia and industry. Still, CFD has its limitations and being aware of these are important if it is to be used. Simulations of complex flows need to be validated with experiments or tests to ensure that results are accurate enough and can be trusted.

In this thesis, two common and well documented heat exchanger geometries have been modelled and simulated in Siemens Star-CCM+, a commercial CFD software. Both are circular tube heat exchangers, one with continuous flat fins and one without fins. The heat exchanger geometries are taken from the book *Compact Heat Exchangers* (1984) by William M. Kays and Alexander L. London. This book contains experimental data for a wide range of heat exchanger designs. Simulations are validated by comparing two key performance parameters for heat exchangers to the experimental data. These are the Fanning friction factor (flow friction performance) and the Colburn j-factor (thermal performance).

The purpose of this thesis is not only to develop a validated simulation model, but to make a more comprehensive study of the methodology and approach to simulating heat exchangers. Examples of questions that arise are: What is the best

way to model the computational domain for heat exchanger simulations? What recommendations can be made regarding solvers and turbulence models? What other recommendations can be made regarding more detailed setup settings? These question have been investigated by initially doing a literature review looking at previous papers on CFD of heat exchangers, followed by the development of in-house simulation models. Achieving accurate results that correlate to experimental values is the main goal, but real-life simulation time and numerical stability is also taken in to account when assessing methods.

1.2 Limitations

In this thesis, only Reynolds-Averaged-Navier-Stokes (RANS) turbulence models have been used in simulations. Other techniques such as Large Eddy Simulations (LES) or Direct Numerical Simulations (DNS) have not been investigated. Simulations have only been run and validated within Reynolds numbers where experimental data exists ($Re \approx 900 - 14000$ for the tube bundle geometry, and $Re \approx 500 - 8000$ for the fin-tube geometry). Simulations have only been made using Siemens Star-CCM+ and the work is therefore limited to using models and solvers available in this software. Only the air side performance of the heat exchangers have been analysed.

2

Theory

2.1 Governing Equations of CFD

CFD codes solve problems related to fluid flow and heat transfer by discretizing a set of governing equations over finite control volumes of the computational domain, often called elements or cells. These elements represent the smallest possible fluid element where microscopic behaviour between individual molecules can be ignored. Mathematically, they are defined as three dimensional volumes with lengths δx, δy and δz. This section introduces these governing equations. The notation and theory of this section is based on that of the Siemens StarCCM+ theory guide (Siemens Digital Industries Software, 2025).

2.1.1 Conservation of Mass

Conservation of mass states that the increase of mass within a control volume is equal to the net flux of mass through its faces. It is expressed through the continuity equation

$$\frac{\partial \rho}{\partial t} + \nabla \cdot (\rho \boldsymbol{u}) = 0 \tag{2.1}$$

where ρ is the density and $\boldsymbol{u}$ is the velocity vector. For incompressible flows the density is constant, simplifying the equation to

$$\nabla \cdot \boldsymbol{u} = 0 \tag{2.2}$$

2.1.2 Conservation of Linear Momentum

Conservation of linear momentum, also known as the Navier-Stokes equations, states that rate of change of linear momentum is equal to the sum of forces acting on the control volume.

$$\frac{\partial (\rho \boldsymbol{u})}{\partial t} + \nabla \cdot (\rho \boldsymbol{u} \otimes \boldsymbol{u}) = -\nabla \cdot (p\boldsymbol{I}) + \nabla \cdot \boldsymbol{T_{visc}} + \boldsymbol{f_b} \tag{2.3}$$

Here, $\boldsymbol{I}$ is the identity matrix and $\boldsymbol{f_b}$ represent the body forces. The viscous stress tensor is denoted by $\boldsymbol{T_{visc}}$ and for a compressible Newtonian fluid it is given by

$$\boldsymbol{T_{visc}} = \mu \left(\nabla \boldsymbol{u} + (\nabla \boldsymbol{u})^T - \frac{2}{3} (\nabla \cdot \boldsymbol{u}) \boldsymbol{I} \right) + \zeta (\nabla \cdot \boldsymbol{u}) \boldsymbol{I} \tag{2.4}$$

where μ is for the dynamic viscosity and ζ the bulk viscosity. For an incompressible fluid the density becomes constant and the importance of bulk viscosity disappear. This simplifies Eq.2.3 to

$$\rho\left(\frac{\partial \boldsymbol{u}}{\partial t} + \nabla \cdot (\boldsymbol{u} \otimes \boldsymbol{u})\right) = -\nabla \cdot (p\boldsymbol{I}) + \nabla \cdot \left(\mu\left(\nabla \boldsymbol{u} + (\nabla \boldsymbol{u})^T\right)\right) + \boldsymbol{f_b} \tag{2.5}$$

2.1.3 Conservation of Energy

Conservation of energy can be expressed by applying the first law of thermodynamics to a control volume. The general compressible form of this equation is given as

$$\frac{\partial(\rho E)}{\partial t} + \nabla \cdot (\rho E \boldsymbol{u}) = -\nabla \cdot (\boldsymbol{u} \cdot p\boldsymbol{I}) + \nabla \cdot (\boldsymbol{u} \cdot \boldsymbol{T_{visc}}) + \boldsymbol{f_b} \cdot \boldsymbol{u} - \nabla \cdot \boldsymbol{q} + S_E \tag{2.6}$$

where E is the total energy per unit mass and S_E represents an energy source (per unit volume). The $\boldsymbol{q}$ is the heat flux given as

$$\boldsymbol{q} = -k\nabla T \tag{2.7}$$

where the thermal conductivity is denoted by k, and T is temperature. For an incompressible version of Eq. 2.6, the density becomes constant and the viscous stress tensor simplifies as in Eq. 2.5.

2.2 Numerical Methods and Solvers

To numerically solve the governing equations they have to be discretized and applied to each cell/control volume of a finitely subdivided computational domain (Siemens Digital Industries Software, 2025). When it comes to this numerical side of CFD, the goal is to generate algebraic relations that can accurately and effectively represent the original governing partial differential equations (CFD Online, 2012). There are many different methods/discretization techniques available for this. A very common and versatile approach, utilized in many CFD codes specifically, is the Finite Volume Method (FVM). Apart from the already mentioned sources, theory in this section has also been based on that of the book by Versteeg and Malalasekera (2007, Chs. 4–5)

2.2.1 Finite Volume Method

The first step in FVM is to divide the domain into the finite non-overlapping control volumes, or cells. Together all these cells make up the mesh of the domain. In Siemens StarCCM+ a so called co-located grid approach for the mesh is implemented. The particular thing with this approach is that all the dependent flow variables are stored in the cell-centers. The boundaries of the cells are referred to as faces and even though a cell sometimes is referred to as a control volume the FVM can be applied to 1, 2 or 3-dimensional type situations. If a cell boundary would coincide with a domain boundary, and thus not have any neighbouring cell,

a set boundary condition has to be applied to close the system mathematically. In Figure 2.1 a visualization on how a section of a simple 2D mesh could look like is presented, with notation according to Versteeg and Malalasekera (2007, Chs. 4–5)

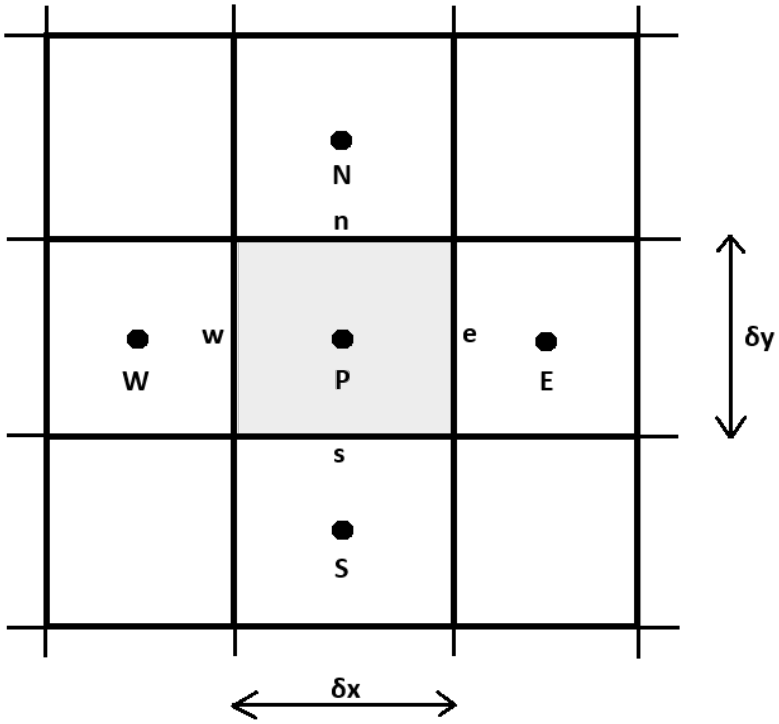

Figure 2.1: Example of a simple 2D mesh section with neighbouring cells. Upper case letters indicates cell-centers and lower case letters indicate faces.

The second step is to reformulate the governing equations from differential form to integral form by integrating them over each cell. After then also applying the Gauss theorem to convert volume integrals containing divergence terms into surface integrals over each cell face, something similar to Eq. 2.8 is achieved.

$$\frac{d}{dt}\int_V \rho\phi dV + \int_S \rho \boldsymbol{u}\phi \cdot d\boldsymbol{S} = \int_S \Gamma \nabla\phi \cdot d\boldsymbol{S} + \int_V S_\phi dV \tag{2.8}$$

Here, V is the volume of the cell, S is a cell-face, $\boldsymbol{S}$ is the cell-face vector and ϕ is an arbitrary transport variable. Going from left to right the first transient term can be disregarded if steady-state, the next surface integral term represents the convective flux, and the second surface integral represents the diffusive flux (note that Γ is an arbitrary diffusive coefficient). Lastly, the last volume integral is the source term.

The next critical step in the FVM is to evaluate the surface flux terms at the cell faces. Since everything is stored in the cell-centers they have to be allocated to the faces. To do this, data stored in neighbouring cell-centers are used to help estimate gradients and interpolate the values. Many methods, or differencing schemes as they often are referred to, have been developed for this. They all vary in robustness, order

of accuracy and suitability for different CFD cases. The easiest approach is to assume a linear variation of the values between the neighbouring cell-centers and thus utilize linear approximation/interpolation. But there are many approaches, some differencing scheme examples include, Central Differencing (linear approximation), 1st order Upwind, 2nd order Upwind, the QUICK scheme, and so on.

After evaluating the face fluxes and interpolating all the variables with, either linear or higher order algebraic approximations, the final discretized governing equations are derived. These are then applied to each cell and solved iteratively using different techniques.

$$a_P \phi_P = \sum a_i \phi_i + S_u \tag{2.9}$$

The equation above (Eq. 2.9) is an example of how a discretized version of a governing equation can look like. The subscript P refers to the current cell-center and i refers to an arbitrary neighbouring cell-center. The a-coefficients contain all the contributions from the diffusive terms, convective terms, variables that have resulted from discretizing, and so on. Lastly S_u is the source term.

2.2.2 Coupled solver

The coupled solver implemented in Siemens StarCCM+ is a density-based solver (Obiso, 2023). This approach solves the governing equations for continuity, momentum and energy (and optionally species) transport at the same time and over the whole domain within each iteration step. This, as opposed to the pressure-based segregated solver which rely on pressure-velocity coupling algorithms like SIMPLE to solve each equation one by one. The coupled solver couples the equations as a vector of equations (Siemens Digital Industries Software, 2025) with the density calculated from the equation of state. Due to the fact that pressure and momentum are solved simultaneously in this large system of algebraic equations, they become tightly connected. This usually means that this kind of solver converge after fewer iterations. But, since it has to store more information each iteration, it requires larger memory (Johansson, 2021). Due to the coupled nature of the governing equations this type of solver are best suited for high speed compressible flows, where large gradients are present, and flow involving complex geometries. On the other hand, as a consequence of this, the solver becomes numerically stiff for low Mach/incompressible flows (usually more suitable for pressure-based solvers) due to large convective and acoustic time-scale separation (Weiss & Smith, 1995).

However, in Siemens StarCCM+ a remedy to this drawback has been implemented to make the density-based coupled solver applicable for low speed flows as well. This is called preconditioning and when enabled (as it is by default) what it does is to mathematically "normalize" the time-scales of the acoustic and momentum information propagation. Put simply, it multiplies the system of equations by a so called preconditioning matrix, see the Siemens theory guide for the exact details (Siemens Digital Industries Software, 2025). This reduces the time-scale separation and thus the numerical stiffness.

Lastly, to march towards the solution, the coupled solver uses a pseudo-time step approach. This approach can vary depending on what type of time dependence the simulation has (Johansson, 2021). For a steady state approach, an inner pseudo-time step (derived by stability constraints) is used to converge an unsteady form of the governing equations to a satisfactory steady state solution for each iteration.

2.3 RANS and Turbulence Modelling

The notation and theory of this section is based on that of the Siemens StarCCM+ theory guide (Siemens Digital Industries Software, 2025) and turbulence model documentation from SimScale (SimScale GmbH, 2023, 2025).

A majority of fluid problems that are analysed numerically involve turbulent flows. Turbulent flows involve quick fluctuations of flow properties such as velocity and thus solving it directly is highly computationally expensive. To reduce computational cost, averaging methods are used to model turbulence. In Reynolds-Averaged Navier–Stokes (RANS), flow properties are decomposed into their mean and fluctuating components

$$\phi = \overline{\phi} + \phi' \tag{2.10}$$

where $\overline{\phi}$ is the averaged mean value and ϕ' is the fluctuating part. In steady state RANS, one can think of the averaging as a time-average. This means that the time dependence of the mean flow disappears. In Unsteady Reynolds-Averaged Navier-Stokes (URANS) however, the averaging process can instead be likened to ensemble-averaging. In URANS turbulence is still modelled, as in a steady state scenario. But keeping the transient terms of the governing equations allows for the possibility to capture large unsteady flow structures such as vortex shedding.

Substituting the RANS decomposition from Eq. 2.10 into the governing equations and averaging yields the general RANS equations

$$\frac{\partial \rho}{\partial t} + \nabla \cdot (\rho \overline{\boldsymbol{u}}) = 0 \tag{2.11}$$

$$\frac{\partial (\rho \overline{\boldsymbol{u}})}{\partial t} + \nabla \cdot (\rho \overline{\boldsymbol{u}} \otimes \overline{\boldsymbol{u}}) = -\nabla \cdot (\overline{p} \boldsymbol{I}) + \nabla \cdot \overline{\boldsymbol{T_{visc}}} + \nabla \cdot \boldsymbol{T_{RANS}} + \boldsymbol{f_b} \tag{2.12}$$

$$\frac{\partial (\rho \overline{E})}{\partial t} + \nabla \cdot (\rho \overline{E}\, \overline{\boldsymbol{u}}) = -\nabla \cdot (\overline{p}\, \overline{\boldsymbol{u}}) + \nabla \cdot (\overline{\boldsymbol{u}} \cdot \overline{\boldsymbol{T_{visc}}}) + \nabla \cdot (\overline{\boldsymbol{u}} \cdot \boldsymbol{T_{RANS}}) - \nabla \cdot \overline{\boldsymbol{q}} + \boldsymbol{f_b} \cdot \overline{\boldsymbol{u}} + S_E \tag{2.13}$$

One can note that these equations closely resemble the original governing equations, with the exception of one directly resulting extra term. This new term is the so called Reynolds stress tensor, $\boldsymbol{T_{RANS}}$.

$$\boldsymbol{T_{RANS}} = -\rho \begin{bmatrix} \overline{u'u'} & \overline{u'v'} & \overline{u'w'} \\ \overline{v'u'} & \overline{v'v'} & \overline{v'w'} \\ \overline{w'u'} & \overline{w'v'} & \overline{w'w'} \end{bmatrix} \tag{2.14}$$

This tensor contains the Reynolds stresses which are the cause of the so called closure problem of the RANS equations. In other words, there are now more unknowns than equations. The Reynolds stresses need to be estimated using mathematical models. This is where the turbulence modelling comes into the picture.

In simple terms, a turbulence model tries to approximate the average influence that the unresolved turbulent fluctuations has on the mean flow, and there are different approaches to this. The turbulence models included in this thesis, however, belong to the family of eddy-viscosity models. They are characterised by using the so called Boussinesq hypothesis which assumes that the Reynolds stresses relates linearly to the mean strain rate tensor via an enhanced viscosity coefficient called eddy/turbulent viscosity, μ_t. This allows the Reynolds stress tensor to be decomposed into one shear related (deviatoric) part and another normal stress related (isotropic) part. Note that the following equation is written to capture a general compressible flow. This means a second isotropic term are also included that accounts for compressibility effects. This term disappears for incompressible flows.

$$\boldsymbol{T_{RANS}} = \left[\mu_t \left(\nabla \overline{\boldsymbol{u}} + (\nabla \overline{\boldsymbol{u}})^T\right)\right]_{deviatoric} - \left[\frac{2}{3}\rho k \boldsymbol{I} + \frac{2}{3}(\mu_t \nabla \cdot \overline{\boldsymbol{u}})\boldsymbol{I}\right]_{isotropic} \tag{2.15}$$

Here, k in the normal stress related isotropic term is the Turbulent Kinetic Energy (TKE). The eddy-viscosity models then solve additional transport equations for different scalar properties (one or more), depending on what turbulence model it is, that makes it possible for μ_t to be derived.

Furthermore, the assumption of a linear relation by the Boussinesq hypothesis comes with its limitations when accounting for turbulence anisotropy and aggressive stream-wise curvature. To help account for this, the linear approximation can also be extended to various degrees of non-linear relations. In Siemens StarCCM+ (Siemens Digital Industries Software, 2025) this has been implemented for some turbulence models (k-omega and standard k-epsilon) as a quadratic and a cubic constitutive option.

2.3.1 k-epsilon, two-layer

The standard k-epsilon turbulence model is a common two-equation based, eddy-viscosity model. It solves transport equations for TKE (k) and turbulent dissipation rate (ϵ) to determine μ_t, see Eq. 2.16 and 2.17 (written according to Siemens Digital Industries Software, 2025). The two-layer approach, an alternative to the more common low Reynolds approach, also allows the model to be applied within the viscous-affected layer close to the wall without relying on wall functions. This makes the model compatible with using both a low Reynolds type mesh ($y^+ \sim 1$) or

a wall function type mesh ($y^+ > 30$). The computations become divided into two layers, one far from the wall where the transport equations are solved as usual and another layer close to the wall where ϵ and μ_t become functions of wall distance. The values from the close wall region then gets blended smoothly with the outer layer values.

$$\frac{\partial(\rho k)}{\partial t} + \nabla \cdot (\rho k \overline{\boldsymbol{u}}) = \nabla \cdot \left[\left(\mu + \frac{\mu_t}{\sigma_k} \right) \nabla k \right] + P_k - \rho(\epsilon - \epsilon_0) + S_k \tag{2.16}$$

$$\frac{\partial(\rho \epsilon)}{\partial t} + \nabla \cdot (\rho \epsilon \overline{\boldsymbol{u}}) = \nabla \cdot \left[\left(\mu + \frac{\mu_t}{\sigma_\epsilon} \right) \nabla \epsilon \right] + \frac{1}{T_e} C_{\epsilon 1} P_\epsilon - C_{\epsilon 2} \rho \left(\frac{\epsilon}{T_e} - \frac{\epsilon_0}{T_0} \right) + S_\epsilon \tag{2.17}$$

The eddy viscosity is then solved on its standard form as Eq. 2.18. For the exact two-layer mathematical formulation implemented in Siemens StarCCM+ see the theory guide (Siemens Digital Industries Software, 2025).

$$\mu_t = \rho C_\mu \frac{k^2}{\epsilon} \tag{2.18}$$

The new model parameters in Eq. 2.16, 2.17 and 2.18 are described in Table 2.1 below.

Table 2.1: Description of standard two-layer k-epsilon parameters

Parameter	**Description**
C_μ	Model coefficient
T_e	$= \frac{k}{\epsilon}$, the large-eddy time scale
σ_k	Model coefficient
σ_ϵ	Model coefficient
$C_{\epsilon 1}$	Model coefficient
$C_{\epsilon 2}$	Model coefficient
P_k	Production term
P_ϵ	Production term
S_k	Source term
S_ϵ	Source term
ϵ_0	Ambient turbulence value in the source terms, counteracts turbulence decay
T_0	Specific time scale stemming from the addition of an ambient source term

The exact definitions of the model parameters can be found in the Siemens k-epsilon turbulence theory guide (Siemens Digital Industries Software, 2025).

The standard k-epsilon model is generally applied for free-shear flow cases without large separation and reattachment. It is not recommended for complex flow with large curvatures or strong adverse pressure gradients. Even though Siemens StarCCM+ allows for the model to be configured with a two-layer or a Low-Reynolds approach, the wall function configuration is still generally preferred configuration.

2.3.1.1 Realizable k-epsilon, two layer

The Realizable k-epsilon turbulence model builds on the standard k-epsilon variant but have two main differences. The first difference being how the eddy viscosity is solved.

$$\mu_t = \rho C_\mu f_\mu \frac{k^2}{\epsilon} \tag{2.19}$$

The exact model dependant formulation of Eq. 2.19 can be found in Siemens Digital Industries Software, 2025. Here, a damping function (f_μ) have been added which means that C_μ is no longer a constant like in the standard k-epsilon but a function of mean flow and turbulence properties. The second difference is a modified transport equation for the dissipation rate (ϵ).

$$\frac{\partial(\rho\epsilon)}{\partial t} + \nabla \cdot (\rho\epsilon\overline{\boldsymbol{u}}) = \nabla \cdot \left[\left(\mu + \frac{\mu_t}{\sigma_\epsilon}\right)\nabla\epsilon\right] + \frac{1}{T_e}C_{\epsilon 1}P_\epsilon - C_{\epsilon 2}f_2\rho\left(\frac{\epsilon}{T_e} - \frac{\epsilon_0}{T_0}\right) + S_\epsilon \tag{2.20}$$

Here the addition of another damping function (f_2) has been added

$$f_2 = \frac{k}{k + \sqrt{\nu\epsilon}} \tag{2.21}$$

where ν is the kinematic viscosity. These additions and also the fact that the definition of P_ϵ is changed (Siemens Digital Industries Software, 2025) is what makes the model "Realizable". In short it means that the model now satisfy additional mathematical constraints on the Reynolds normal stresses, making it more consistent with physics of turbulent flows, by removing the possibilities of negative values for these.

This model is described by both Siemens Digital Industries Software, 2025 and SimScale GmbH, 2023 to be a improved (or as good as) version of the standard k-epsilon turbulence model for many flow cases. This includes flow cases with separation and recirculation. In Siemens StarCCM+ it is compatible with a two layer configuration, which also is the software default k-epsilon turbulence model.

2.3.2 Standard Elliptic Blending k-epsilon

The Elliptic Blending (EB) turbulence models can be viewed as an even further development of the k-epsilon model. To solve the eddy-viscosity it uses, in its standard form, four transport equations. The first two solve for k and ϵ, hence the connection to the k-epsilon model. The other two transport equations solve for the so called normalized wall-normal stress component (φ) and the elliptic blending factor (α).

$$\frac{\partial(\rho k)}{\partial t} + \nabla \cdot (\rho k\overline{\boldsymbol{u}}) = \nabla \cdot \left[\left(\frac{\mu}{2} + \frac{\mu_t}{\sigma_k}\right)\nabla k\right] + P_k - \rho(\epsilon - \epsilon_0) + S_k \tag{2.22}$$

$$\frac{\partial(\rho\epsilon)}{\partial t} + \nabla \cdot (\rho\epsilon\overline{\boldsymbol{u}}) = \nabla \cdot \left[\left(\frac{\mu}{2} + \frac{\mu_t}{\sigma_\epsilon}\right)\nabla\epsilon\right] + \frac{1}{T_e}C_{\epsilon 1}P_\epsilon - C^*_{\epsilon 2}\rho\left(\frac{\epsilon}{T_e} - \frac{\epsilon_0}{T_0}\right) + S_\epsilon \tag{2.23}$$

$$\frac{\partial(\rho\varphi)}{\partial t} + \nabla \cdot (\rho\varphi\overline{\boldsymbol{u}}) = \nabla \cdot \left[\left(\frac{\mu}{2} + \frac{\mu_t}{\sigma_\varphi}\right)\nabla\varphi\right] + \rho\frac{\epsilon_0\varphi_0}{k_0} + P_\varphi + S_\varphi \tag{2.24}$$

$$\nabla \cdot (L^2\nabla\alpha) = \alpha - 1 \tag{2.25}$$

φ is furthermore defined as

$$\varphi = \frac{\overline{u_n^2}}{k} \tag{2.26}$$

where u_n is the wall-normal fluctuating velocity. Lastly, the eddy-viscosity is calculated according to Eq. 2.27

$$\mu_t = \rho C_\mu \varphi k \; min\left(\sqrt{T_e^2 + C_t^2\frac{\nu}{\epsilon}},\; \frac{C_T}{\sqrt{3}C_\mu\varphi S}\right) \tag{2.27}$$

All model parameters are described in Table 2.2 below. Exact mathematical definitions can be found in the EB k-epsilon theory from the Siemens guide Siemens Digital Industries Software, 2025.

Table 2.2: Description of the standard EB k-epsilon parameters

Parameter	**Description**
P_k	Production term
P_ϵ	Production term
P_φ	Production term
L	Turbulent length-scale
$C_{\epsilon 1}$	Model coefficient
$C^*_{\epsilon 2}$	Model coefficient
σ_k	Model coefficient
σ_ϵ	Model coefficient
σ_φ	Model coefficient
C_T	Model coefficient
C_t	Model coefficient
C_μ	Model coefficient
T_e	$= \frac{k}{\epsilon}$, the large-eddy time scale
S_k	Source term
S_ϵ	Source term
S_φ	Source term
k_0, ϵ_0 and φ_0	Ambient turbulence values that counteracts turbulence decay
ν	Kinematic viscosity
S	Modulus of the mean strain rate tensor

The concept of elliptic relaxation was first proposed by Durbin, 1993 and is basically an attempt to, in a non-local and improved way, tackle the fact that turbulence can behave strongly non-homogenous/anisotropic in the presence of walls. In comparison to regular two equation k-epsilon models, these near-wall regions are often simplified and captured on a local level using empirical solutions (damping functions

etc.). The elliptic relaxation concept has then been further developed into the more industry friendly EB models, such as the one implemented by Siemens StarCCM+ and described in this section. The standard EB k-epsilon model is based on the model developed by Billard and Laurence, 2012 with some slight tweaks mainly for stability reasons, see (Siemens Digital Industries Software, 2025). According to the Siemens theory guide this model is a truly robust model for complex flow geometries (recirculation, separation etc.). It is summarized as an improvement over the Realizable k-epsilon model in terms of accuracy and an improvement over the SST k-omega model in terms of stability.

2.3.3 SST k-omega

The k-omega turbulence model, first proposed by Wilcox, 1988, is another very common two-equation based, eddy-viscosity model. One large advantage of this model compared to that of the standard k-epsilon is that it can be integrated over the whole boundary layer without relying on the use of any wall or damping functions in the near-wall region. This is provided that a low Reynolds style mesh ($y^+ \sim 1$) is used. On the flip side, in its standard configuration it becomes very sensitive to free stream values and turbulent inlet boundary conditions. This is the biggest drawback of the standard k-omega model since it is known to easily over predict and cause early separation according to SimScale GmbH, 2025. For this reason, the Shear-Stress-Transport (SST) k-omega model was developed (Menter, 1994). In short, what it does is to combine the k-epsilon type behaviour in the free stream region far from the wall and blend it with the k-omega type behaviour in the near-wall region using so called blending functions. The transport equations that the SST k-omega model solves are, according to Siemens Digital Industries Software, 2025, defined as

$$\frac{\partial(\rho k)}{\partial t} + \nabla \cdot (\rho k \overline{\boldsymbol{u}}) = \nabla \cdot [(\mu + \sigma_k \mu_t) \nabla k] + P_k - \rho \beta^* (\omega k - \omega_0 k_0) + S_k \tag{2.28}$$

$$\frac{\partial(\rho \omega)}{\partial t} + \nabla \cdot (\rho \omega \overline{\boldsymbol{u}}) = \nabla \cdot [(\mu + \sigma_\omega \mu_t) \nabla \omega] + P_\omega - \rho \beta (\omega^2 - \omega_0^2) + S_\omega \tag{2.29}$$

where the new term omega (ω) is called the specific turbulent dissipation rate.

$$\omega \propto \frac{\epsilon}{k} \tag{2.30}$$

The other model parameters in Eq. 2.28 and 2.29 are described in Table 2.3 below. Exact mathematical and model dependent formulations can be found in Siemens Digital Industries Software, 2025.

Table 2.3: Description of the SST k-omega parameters

Parameter	Description
σ_k	Model coefficient
σ_ω	Model coefficient
β^*	Model coefficient
β	Model coefficient
P_k	Production term
P_ω	Production term
S_k	Source term
S_ω	Source term
ω_0 and k_0	Ambient turbulence values to counteracts turbulence decay

The eddy viscosity in the SST k-omega model is calculated according to Eq. 2.31. Note that this equation is written on its standard form and the exact formulation of it used by Siemens StarCCM+ is found in the Siemens theory guide (Siemens Digital Industries Software, 2025).

$$\mu_t = \frac{a_1 \rho k}{max(a_1 \omega,\ SF_2)} \tag{2.31}$$

The parameter a_1 is a model coefficient, S is the modulus of the mean strain rate tensor and F_2 is one of the blending functions. As its name suggest the blending functions job is to smoothly blend the k-epsilon and k-omega models based on wall distance. Another blending function exist within the transport equation for ω, once again see (Siemens Digital Industries Software, 2025).

The SST k-omega model is a very versatile turbulence model and the one used the most as an industry standard (SimScale GmbH, 2025). It is often better and more accurate at capturing flow separation compared to other RANS models and performs well under adverse pressure gradients. The model is also relatively computationally cheap. One negative however is that it has shown to sometimes over-predict turbulence in stagnation and aggressive acceleration regions where normal strain is large.

2.3.4 Transition modelling

Transition within the context of fluid flow modelling is, put simply, when the flow within a boundary layer turns from laminar to turbulent behaviour. This can be induced in different ways depending on flow conditions, geometry and external disturbances. Natural transition is when a laminar boundary layer gradually turns turbulent ”by itself” due to flow instabilities getting larger and larger as the flow reaches beyond a certain ”critical” Reynolds number. Transition can also be induced by flow separation. Adverse pressure gradients (if large enough) cause the laminar boundary layer to detach, forming a recirculation/separation region. This triggers transition within the highly unstable separated shear layer between this separation region and the free stream region. Another mechanism is by-pass transition. This is when turbulence in the incoming free stream flow, caused for example by some

external disturbance, are large enough to directly interact with the boundary layer and drive the transition. Surface roughness is yet another example of a transition inducing factor that often affect and accelerates the onset of transition.

Most standard turbulence models by themselves are built on the assumption of fully turbulent flow. Therefore, extra so called transition models are required if boundary layer transition behaviour is to be captured. There are some exceptions to this. Some turbulence models such as the extended low Reynolds (and two layer) k-epsilon models (that use damping functions or other near-wall mathematical solutions) can artificially mimic and capture transition to some extent. Another example of this is the EB k-epsilon model which does this even further. When it comes to the k-omega model, this is generally not the case. Therefore that model is often paired with some sort of additional transition model.

Numerous transition model variants exist and in Siemens StarCCM+, three are implemented. The least computationally heavy option is the Turbulence Suppression model which just suppresses turbulence in certain user-defined areas. This requires the user to know where these areas should be in advance however. The other two options operate on a more predicting/solving level. These are the so called Gamma Transition model and the more computationally expensive Gamma-ReTheta model. It is specifically common for the SST k-omega turbulence to be combined with either of these Gamma based models (Siemens Digital Industries Software, 2025). The coupling is done by modifying the turbulence transport equations for TKE (k) and specific dissipation rate (ω) and a modified TKE production term (P_k). See the theory guide (Siemens Digital Industries Software, 2025) for the exact formulations of the modified/updated transport equations.

2.3.4.1 The Gamma-ReTheta model

This transition model builds on the concept of intermittency (γ) which is a measurement on how much of the time the flow is turbulent. An intermittency value of 1 means that the flow is fully turbulent and a value of 0 means that the flow is fully laminar (at all times). In other words, the intermittency control how much the turbulence model should be dampened.

During its development, the principle with the Gamma-ReTheta model was to provide a transition model that was able to be based more on local flow variables, thus making it easier to be implemented in modern (unstructured) CFD codes. In short it uses a combination of transport equations together with empirical correlations rather than any free-stream based boundary-layer calculations. It is also an extension on the more simple, single equation, Gamma transition model. While that model only solves one transport equation for intermittency, the Gamma-ReTheta model is extended into a two equation variant, see Eq. 2.32 and 2.33. In this additional equation, a semi-local approach is used since it takes the transition onset momentum thickness Reynolds number ($Re_{\theta t}$) evaluated using empirical correlations in the free-stream, and propagates it into the boundary layer using a transport equation with local flow variables. The role of this equation is then to indicate where

the onset of transition should occur in the boundary layer.

$$\frac{\partial(\rho\gamma)}{\partial t} + \nabla \cdot (\rho\gamma\overline{\boldsymbol{u}}) = \nabla \cdot \left[\left(\mu + \frac{\mu_t}{\sigma_f}\right)\nabla\gamma\right] + P_\gamma - E_\gamma \tag{2.32}$$

$$\frac{\partial(\rho\overline{Re_{\theta t}})}{\partial t} + \nabla \cdot (\rho\overline{Re_{\theta t}}\overline{\boldsymbol{u}}) = \nabla \cdot \left[\sigma_{\theta t}\left(\mu + \mu_t\right)\nabla\overline{Re_{\theta t}}\right] + P_{\theta t} + D_{SCF} \tag{2.33}$$

For the exact formulations of the parameters in Eq. 2.32 and 2.33 see Siemens theory guide (Siemens Digital Industries Software, 2025). A brief explanation can be found in Table 2.4 below.

Table 2.4: Description of the Gamma-ReTheta parameters

Parameter	Description
γ	Intermittency
$\overline{Re_{\theta t}}$	Transition momentum thickness Reynolds number
f_μ	Damping function
σ_f	Model coefficient
σ_{thetat}	Model coefficient
σ_ϵ	Model coefficient
P_γ	Production term
E_γ	Destruction/relaminarization term
$P_{\theta t}$	Production term
D_{SCF}	Cross-flow term

In Siemens StarCCM+, the Gamma-ReTheta model is by default a fully correlation based model. This means that the transition onset and development are governed by pre-defined empirical correlations. Manually calibrating the model is not an easy task and therefore default correlations have been provided by Siemens StarCCM+ (the option to tweak them are still available however). For the exact correlations used and implemented by Siemens, see the Gamma-ReTheta theory guide (Siemens Digital Industries Software, 2025).

2.4 Dimensionless Numbers

Dimensionless numbers are common within fluid dynamics and thermodynamics and are used to analyse and compare flow behaviour and heat transfer. The following section describes the most central dimensionless numbers used in this thesis. The theory and definitions are taken from White, 2011 and Bergman, 2020.

2.4.1 Reynolds Number

The Reynolds number is a dimensionless number describing the ratio of inertial forces to viscous forces in a fluid.

$$Re = \frac{\rho V L}{\mu} \tag{2.34}$$

Where ρ is the density of the fluid, V is the freestream velocity of the fluid, L is the characteristic length and μ is the dynamic viscosity of the fluid. The Reynolds number is important as it is used to predict flow behaviour and transition from laminar to turbulent flow.

2.4.2 Prandtl Number

The (molecular) Prandtl number describes the ratio of momentum diffusivity over thermal diffusivity in a fluid. In other words, the propagation of momentum over the propagation of heat. It is determined purely from fluid properties

$$Pr = \frac{\mu c_p}{k} \tag{2.35}$$

where c_p is the specific heat of the fluid and k is the thermal conductivity.

2.4.3 Turbulent Prandtl Number

The turbulent Prandtl number differs from the previously mentioned molecular Prandtl number. As described by Li, 2019, this number is the ratio between eddy viscosity (μ_t) and eddy diffusivity for heat (k_t).

$$Pr_t = \frac{\mu_t c_p}{k_t} \tag{2.36}$$

It is a key parameter for determining how heat spreads compared to momentum in turbulent flows.

2.4.4 Stanton Number

The Stanton number describes the ratio of heat transferred to a fluid to its thermal capacity. It tells how effectively a fluid receives or gives off heat.

$$St = \frac{h}{Gc_p} \tag{2.37}$$

Where h is the heat transfer coefficient and G is the mass velocity.

2.4.5 Colburn j-factor

The Colburn j-factor is a dimensionless heat transfer coefficient. It is a common parameter used for determining the heat transfer performance of compact heat exchangers.

$$j_H = StPr^{2/3} = \frac{h}{Gc_p}(\frac{\mu c_p}{k})^{2/3} \tag{2.38}$$

2.4.6 Fanning friction factor

The Fanning friction factor is defined as the ratio between the local shear stress and the dynamic pressure.

$$f = \frac{\tau}{q} \tag{2.39}$$

Given a geometry, it can be used to derive the pressure loss in a fluid flow or vice versa. It should not be confused with the Darcy friction factor which is four times the Fanning friction factor.

3
Literature Study

A literature study of various papers and studies analysing different heat exchanger configurations is presented in this chapter. Focus has mainly been on understanding and gaining knowledge of different possible CFD modelling approaches, previously used in research. For a more compact summery of this literature review see Table 3.1.

In Bhuiyan et al. (2014) 3D steady state simulations were performed on finned tube heat exchangers using ANSYS CFX12.0. The purpose was to analyse the effect of changes in longitudinal pitch, transverse pitch and fin pitch on performance. The k-omega model was used to model turbulence, as it had shown good correlation to experimental results in previous papers according to the authors. Results were validated to previous experimental data. The computational domain was a single channel of 4 rows of tubes. Symmetry conditions were used on one side, allowing the authors to model only half of the domain. A mesh with approximately 450 000 elements was deemed fine enough to capture the flow accurately. Both a staggered tube configuration and an inline tube configuration were tested. The maximum difference between the experimental data and the numerical results was less than 7% and 12% in the case of friction factor and and Colburn j-factor respectively. Simulations showed that an increase in longitudinal and transverse tube pitch cause a decrease in heat transfer and flow friction performance. On the other hand, a decrease in fin pitch resulted in an increase in performance.

In Lotfi and Sunden (2023) a fin and tube heat exchanger with an inserted ”space-filling structure” in between the fins (also called cellular lattice structures) was analysed. The idea of the inserted structures, consisting of small cubic truss-systems, were to increase mixing and the surface to volume ratio. Different lattice structure configurations of varying porosity were tested. The purpose was to investigate the effect and possible enhancement in the air-side thermal-hydraulic performance. Results showed that the trussed fin and tube exchangers using a lattice truss structure of 92% porosity produced the best results. To test this, 3D conjugate heat transfer simulations in the CFD software ANSYS CFX were carried out. A single channel unit cell approach was utilized where the smallest repeating part of the 3D pattern was modelled. It consisted of three staggered rows of elliptical tubes. The domain was also extended 5 and 20 times the fin spacing in the upstream and downstream directions respectively. The simulations were modelled using steady RANS with the SST k-omega turbulence model. The inlet boundary condition was set to a uniform velocity inlet with a static temperature of 343 K and a turbulence intensity of 5%. For the outlet they used a regular pressure outlet. Both the tube walls and the

trusses were set to no-slip, with the tubes having a constant temperature of 293 K. Symmetry conditions were applied on the domain sides and periodic conditions were applied on the top and bottom of the domain, basically repeating the channel and making it an infinite array of unit cells. The fin and air interfaces were modelled with both temperature and heat flux continuity. The Colburn j-factor and the Fanning friction factor were plotted against the hydraulic Reynolds number. For validation a clean fin and tube heat exchanger, without any inserted structures, was simulated and the Colburn and Fanning friction plots were compared to experimental results from a previous study (Wang et al., 2000). Apart from the SST k-omega model they also investigated the use of a laminar model, and the RNG k-epsilon model. They note however that using the SST k-omega model produces the closest results to the experimental benchmark. Mesh convergence was achieved at around 9 million cells, resulting in a very dense mesh.

A plain fin and tube heat exchanger was studied in an article by Altwieb et al., 2020. The aim was to analyse and understand the air-side performance of this type of heat exchanger. Furthermore, the effect of varying geometry parameters such as fin spacing and tube pitch (longitudinal and transverse) was studied. For this, numerical simulations were carried out and validated against experimental tests, also carried out during the study. The numerical calculations were carried out in the form of steady-state 3D CFD simulations in ANSYS FLUENT (17.0). The full heat exchanger geometry was modelled and used in the computational domain. This included 21 aluminium fins and 10 round copper tubes ordered in a staggered configuration. The heat exchanger had 2 tube rows downstream, each containing 5 tubes. The simulation setup utilized steady-state RANS together with the SST k-omega turbulence model. Hot water was used inside the tubes and air (assumed as an incompressible ideal gas) was used as the external fluid. Sufficient mesh independence was achieved around 8 million cells. The main performance parameters utilized was the Fanning friction factor and the Colburn factor, calculated according to Kays and London, 1984), the fin efficiency was also evaluated per fin (with an average value of around 0.75). Lastly, in the conclusions it was stated that the modelling of a complete heat exchanger geometry, as opposed to using a simplified periodic domain approach, led to an improvement in accuracy when capturing the overall thermal and flow performance.

The paper by Chu et al. (2020) carried out a comparative study of airside performance for sinusoidal wavy-fin and tube heat exchangers with round and oval tubes. The exchangers were tested experimentally, but also numerically (using CFD) to analyse more detailed local heat transfer performance. A variation in fin pitch (1.8-3 mm) and number of tube rows (2-6) was also implemented. The results showed that round tubes produced higher pressure drop at a fin pitch of 3 mm, meanwhile the oval tubes produced a higher pressure drop at a smaller fin pitch of 1.8 mm. The effect of fin pitch on the heat transfer performance was small for the exchangers having between 2-4 rows of tubes. However, the exchangers having 6 tube rows showed that the heat transfer coefficient could be improved approximately 10-20% and 9.3–25.2% for the round and oval tubes respectively, by increasing the fin pitch.

The CFD simulations were carried out using ANSYS Fluent and the numerical set up consisted of a 3D steady segregated solver (SIMPLE algorithm) utilizing RANS SST k-omega for turbulence. The domain was defined as a single channel tube row with one fin in the middle and two air regions connected via a periodic boundary condition on the top and bottom. Symmetry conditions were applied on the left and right boundaries. A velocity inlet and a regular pressure outlet was also used. Further more, extended regions upstream and downstream were also incorporated of 30 mm and 60 mm respectively. The tube walls were given a constant temperature of 60° C to correspond to the experiments. Mesh convergence was achieved at around 5.72 million mesh nodes with residuals reaching bellow 10^{-6}.

An alternative method of modelling flow across a heat exchanger is through fully developed periodic flow in a 1x1 unit cell. The 1x1 unit cell is the smallest possible repeating geometry of a heat exchanger and is thus ideal for minimizing the computational domain. In a paper by Webb and Cook, 2006, results from RANS, URANS and LES simulations of water flow over a tube bundle were compared to previously made experiments. The domain, modelled in FLUENT, was a three dimensional unit cell of the tube bundle geometry with periodic boundary conditions in each direction. A mass flow was specified across the inlet and outlet interface, resulting in a fully developed flow across the tube bundle. The simulated case was water flowing at a speed of 1.02 m/s, resulting in a Reynolds number of 21 000. The RNG k-epsilon turbulence model was used for the RANS and URANS simulations. The same mesh of around 1 000 000 cells was used for all simulations. Plots of the mean velocity gradient in x as well as the turbulent kinetic energy were compared to experimental results. All three models compared well to the mean x-velocity data, with the LES predictions being the better of the three. For turbulent kinetic energy, the RANS model overpredicted the data, while the URANS model underpredicted the data.

Table 3.1: Summary of literature study

Authors, year	**Case**	**Software**	**Computational Domain**	**Setup**	**Mesh**
Lotfi & Sunden, 2023	Air flow over fin and tube HEX with truss structures Re=500 − 3000	ANSYS CFX	3D single channel with 3 tube rows, symmetry & periodic BCs	RANS + SST k-omega	∼9 million cells
Bhuiyan et al., 2014	Air flow over fin and tube HEX, Re=2000-7000	ANSYS CFX	3D single channel with 4 tube rows, symmetry & periodic BCs	RANS + k-omega	∼450 000 cells
Altwieb et al., 2016	Air flow over full fin and tube HEX $Re \sim 5000 - 30000$	FLUENT	Full HEX geometry	RANS + SST k-omega	∼8 million cells
Webb & Cook, 2006	Water flow over tube bundle, Re=21 000	FLUENT	Fully developed periodic unit cell	RANS & URANS + RNG k-epsilon, LES	∼1 million cells
Chu et al., 2020	Air flow over wavy fin and tube HEX Re=2000 − 15000	FLUENT	3D single channel	RANS + SST k-omega	∼5.7 million cells

4
Methods

4.1 Numerical Modelling

The numerical analysis consisted of CFD simulations carried out in the commercial software Siemens StarCCM+. Star-CCM+ is used as it is the more common CFD software used at Chalmers University of Technology. Two heat exchangers have been modelled and simulated, the 8.0-3/8T and S 1.50-1.25, shown in Fig 4.1. Simulating two different types of heat exchanger geometries allows the robustness of the simulation setup to be put to the test, and exposes potential inconsistencies in results.

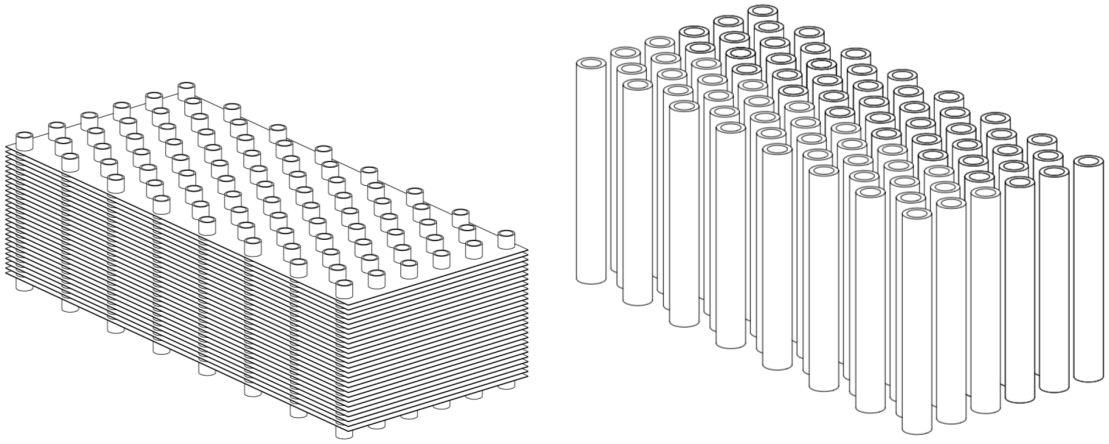

(a) 8.0-3/8T **(b)** S 1.50-1.25

Figure 4.1: 3D visualizations of the heat exchangers. Not to scale.

4.1.1 Computational Domain - Single Channel Approach

In the single channel approach, the heat exchanger domain is reduced to a 3D channel containing the smallest repeating geometrical pattern in Y and Z , see Figure 4.2. In the X direction the channel is extended by multiple tube rows.

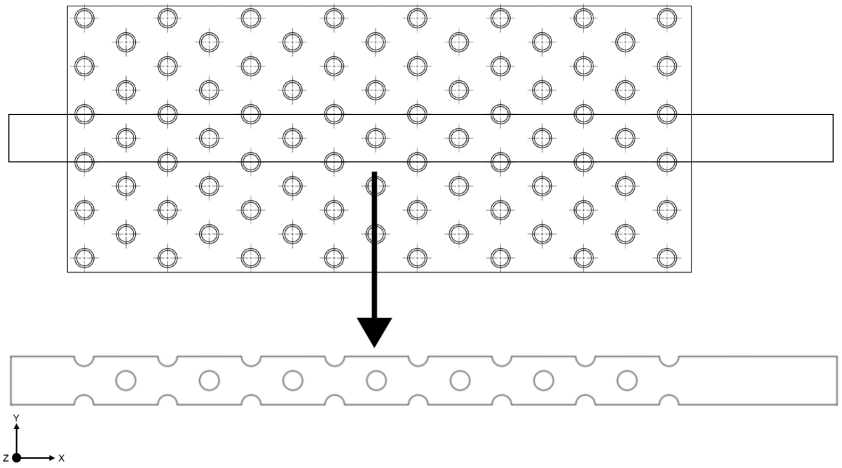

Figure 4.2: Top view of the 8.0-3/8T showcasing the periodicity of the single channel domain.

The left and right side surfaces as well as the top and bottom surfaces are connected through periodic interfaces. The periodic interface corresponds to a repeating pattern of information across the boundaries, meaning that fluxes passing through one boundary are mapped and imposed on the opposite boundary. Using a periodic interface allows one to simulate only a portion of the geometry, which serves as a representative segment of the full model. The channel contains 15 rows of tubes. The reason for having a such a high number of tube rows in the domain is to ensure that the flow is able to fully develop in the core, and to be able to study the effects of the number of tube rows on results. The inlet is placed 30 mm upstream of the heat exchanger to allow fully developed airflow before it reaches the surfaces. The outlet is placed further downstream to reduce circulation and reversed flow across the outlet surface.

4.1.1.1 8.0-3/8T

The 8.0-3/8T heat exchanger consists of staggered circular tubes with continuous fins. The geometrical parameters for the single channel domain is presented in Table 4.1. All parameters are taken from (Kays & London, 1984), except for the number of tubes, the fin heat transfer area, the total heat transfer area and the minimum free-flow area. The heat transfer areas are simply the surface areas of the heat exchanger that are in contact with the air, and have been derived using this definition. The minimum free-flow area is the smallest cross sectional flow-area normal to the air flow in the heat exchanger core, and has been derived using this

definition. A drawing of the domain can be found in Appendix A.

Table 4.1: Geometrical parameters of the 8.0-3/8T single channel

Parameter	Value	Definition	Derivation
W	25.4 mm	Width of channel	-
L	325 mm	Length in flow direction	-
H	3.175 mm	Height of domain (= fin pitch)	-
n	15	Number of full tubes	-
D_t	10.21 mm	Tube diameter	-
p_l	44 mm	Longitudinal tube pitch	-
p_t	12.7 mm	Transverse tube pitch	-
p_f	3.175 mm	Fin pitch	-
t_f	0.3302 mm	Fin thickness	-
A_f	14053 mm^2	Fin heat transfer area	$2(WL - n(0.5D_t)^2\pi)$
A	15420 mm^2	Total heat transfer area	$nD_t\pi \cdot (p_f - t_f) + A_f$
A_c	43.2125 mm^2	Minimum free-flow area	$(W - D_t) \cdot (p_f - t_f)$
D_h	3.6322 mm	Hydraulic diameter	-

The computational domain for the 8.0-3-8T geometry contains 15 rows of tubes in the flow direction. The domain has a "sandwich" layout, with the fin placed in the middle, between the gaps of air below and above, see Figure 4.3.

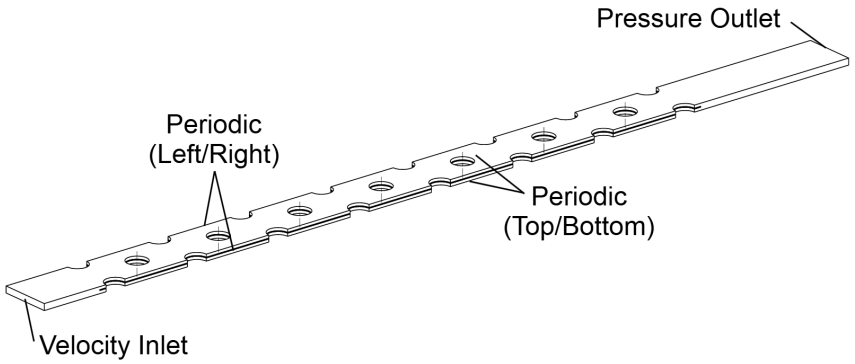

Figure 4.3: Trimetric view of the 8.0-3/8T single channel geometry, with boundary conditions.

4.1.1.2 S 1.50-1.25

The S 1-50-1.25 geometry is a staggered circular tube bundle heat exchanger. The geometrical parameters are found in Table 4.2. Since there is no periodically repeated geometrical pattern in the Z direction, an arbitrary height of 5 mm for the domain was chosen. Periodic BCs are still applies between the top and bottom surface, see Figure 4.4. A drawing of the domain can be found in Appendix B.

Table 4.2: Geometrical parameters of the S 1.50-1.25 single channel

Parameter	Value	Definition	Derivation
W	9.525 mm	Width of channel	-
L	119 mm	Length in flow direction	-
H	5 mm	Height of tubes/domain	-
n	15	Number of full tubes	-
D_t	6.35 mm	Tube diameter	-
p_l	15.875 mm	Longitudinal tube pitch	-
p_t	9.525 mm	Transverse tube pitch	-
A	1496 mm^2	Total heat transfer area	$nD_t\pi H$
A_c	15.875 mm^2	Minimum free-flow area	$(W - D_t) \cdot H$
D_h	5.0292 mm	Hydraulic diameter	-

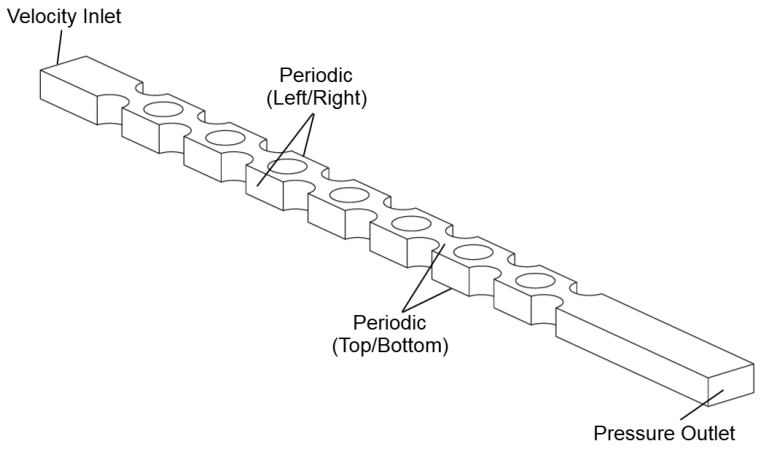

Figure 4.4: Trimetric view of the S 1.50-1.25 single channel geometry, with boundary conditions.

4.1.2 Computational Domain - Unit Cell Approach

The main difference between the single channel approach and the unit cell approach is that the unit cell has periodic boundary conditions in all directions, including between the inlet and outlet. This allows the computational domain to be reduced even further, down to the heat exchangers smallest repeating pattern in every direction, see Figure 4.5. For such a computational domain, the flow exiting the outlet surface has to be mapped on to the inlet surface, creating an ever repeating development that should eventually result in a fully developed flow through the domain. In Star-CCM+ this is done by creating a periodic interface between the inlet and outlet and setting the interface type to *fully developed flow*. For the unit cell approach the fin is separated in half and placed at the top and bottom instead of in the middle as in the single channel domain. This is to avoid having two separate air regions. The geometrical parameters that are unique to the unit cell domain are listed in Table 4.3, the rest are the same as for the single channel domain (Table 4.1). Only the 8.0-3/8T geometry has been simulated using the unit cell approach.

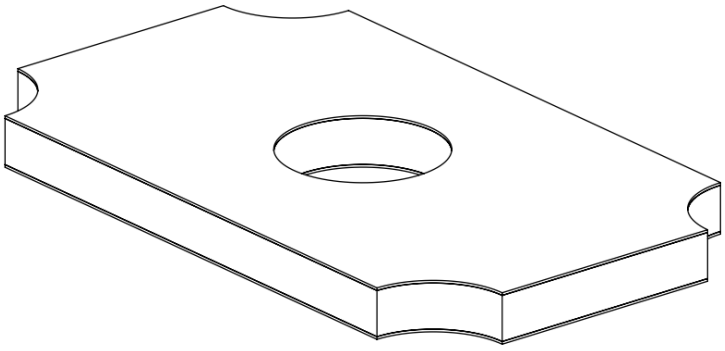

Figure 4.5: Unit cell domain for the 8.0-3/8T

Table 4.3: Unique geometrical parameters of the 8.0-3/8T unit cell

Parameter	Value	Definition	Derivation
L	44 mm	Length in flow direction	-
n	2	Number of full tubes	-
A_f	1907.7 mm^2	Fin heat transfer area	$2(WL - n(0.5D_t)^2\pi)$
A	2090.2 mm^2	Total heat transfer area	$nD_t\pi \cdot (p_f - t_f) + A_f$

4.1.3 Physical and Numerical Setup

The air entering the domain from the inlet surface is controlled by a velocity boundary condition with constant velocity and temperature. Inlet velocities range from approximately 1 m/s to 17.5 m/s. Two types of simulations have been conducted; "cold-core" and "hot-core" simulations. Cold-core simulations have room temperature (300 K) air entering the heat exchanger. The heat exchanger surfaces are 300 K as well, meaning there is no heat transfer happening in the heat exchanger core. These simulations are meant to measure the friction factor as similarly as experiments. In *Compact Heat Exchangers*, additional cold-core experiments were done when measuring the friction factor to remove numerical uncertainties caused by varying temperatures throughout the heat exchanger core (Kays & London, 1984, p.186). In the hot-core case, air enters the domain at 400 K and the tube surfaces are set to 280 K.

The equation of state used for the air is the ideal gas law. The air is defined as incompressible, meaning that the density is not dependent on the working pressure. Sutherland's law is used for determining the dynamic viscosity and thermal conductivity of the air. The specific heat is set at a constant value of 1003.62 J/Kg-K. The turbulent Prandtl number is set to 0.9 (note that this is not the same as the molecular Prandtl number). The turbulence at the inlet and outlet is defined by turbulence intensity and length scale. Turbulence intensity is set to 5% and the length scale is set to 5% of the hydraulic diameter, which are recommended values (CFD Online, 2024, 2025; Lotfi & Sunden, 2023). The outlet boundary condition is a regular pressure outlet with pressure and static temperature set to ambient

conditions (300 K and 1 atm).

The tubes are modelled as wall surfaces of the air domain with a constant temperature applied to them (Kays & London, 1984, p.140, p.188). This allows the tubes to cool or heat the air directly without having to model a second fluid flowing through them. For the finned heat exchanger, the fin is modelled as a separate body in aluminium, with the default StarCCM+ value for thermal conductivity kept (k = 237 W/mK). The fin surfaces are defined as adiabatic walls, with a *conjugate heat transfer* thermal specification for the air-to-fin interface. All walls have no-slip conditions. *Curvature correction* is applied for all turbulence models except for EB k-epsilon, which accounts for the effects on turbulent kinetic energy associated with strong streamline curvatures (Siemens Digital Industries Software, 2025). EB k-epsilon has its own internal approach to handling complex flow geometries.

Although different combinations of solvers and physics settings have been tested and evaluated, the main simulations comparing different turbulence models have been done using a steady state implicit coupled solver, as it has shown better numerical stability and ability to reach a steady state solution compared to a segregated solver. In Star-CCM+, the coupled solver has a property called *preconditioning*. When enabled, it adds a preconditioning matrix when solving the governing equations which reduces the numerical stiffness of the solver for incompressible flows (Siemens Digital Industries Software, 2025). This makes the solver more appropriate for low speed cases despite being a density-based solver.

The turbulence models that have been tested are:

- SST k-omega
- SST k-omega with Gamma-ReTheta transition model
- Realizable k-epsilon (Two layer)
- Elliptic Blending k-epsilon

For every turbulence model, the default Star-CCM+ model coefficients and tuning parameters are kept. For the SST k-omega models, the *Durbin scale-limiter* is kept to help counteract its tendency to over predict turbulence in stagnation and high acceleration regions. This option is not available for the Realizable k-epsilon and the EB k-epsilon since they do this to some extent internally. Lastly, a cubic constitutive option is also enabled for the tube bundle geometry to assist handling of strong streamline curvature in the SST k-omega models. This causes however the finned geometry simulations to become too unstable. For that geometry the default linear constitutive option is kept (since curvature correction is still applied this is assumed alright).

4.1.3.1 Unit Cell Setup

The physical and numerical setup for the unit cell approach is for the most part the same as for the single channel approach, but there are some notable differences. As previously mentioned, the flow in a unit cell type simulation is controlled using a *fully developed flow* interface type, meaning the inlet and outlet boundary conditions

are left untouched since the boundaries get overwritten by the interface. The flow over the domain can be controlled either by imposing a pressure jump across the periodic interface, or by applying a target mass flow rate. Both approaches have been studied in this work. While specifying a target mass flow makes more sense since it most likely will be a known variable when trying to assess a heat exchangers performance, the pressure jump option has notable pros. This is discussed further in Section 5.4.

Energy in the domain is controlled through the fully developed interface as well, using the *constant temperature walls* energy option. With this option a constant temperature is applied to the domain walls, as in the single channel approach. When choosing this option, an *inflow temperature* as well as a *reference temperature* has to be specified. These are set to 400 K and 280 K respectively for the hot-core case. This creates a temperature discontinuity across the periodic interface, allowing heat transfer to be measured. For the cold-core case, the energy option is set to *periodic*, meaning there is no temperature or enthalpy discontinuity at the periodic interface.

4.1.4 Mesh

A polyhedral mesh was utilized due to its capabilities of capturing complex geometries, such as curved surfaces, with a reduced cell-count compared to an equivalent tetrahedral mesh (Siemens Digital Industries Software, 2025). To capture the boundary layer and its effects, a prism layer mesher was also enabled with 8 prism layers. To be compatible with the chosen turbulence models, a low Reynolds mesh approach was employed ($y^+ \sim 1$). The Voulpe y^+-calculator was used to calculate the proper prism layer thickness (Volupe, n.d.). For the exact prism layer settings used for each heat exchanger design, see Table 4.4 and 4.5. With a higher inlet velocity, the y^+-value also gets higher. For the fastest inlet velocities in both geometries, the y^+ never reaches a value above 5 and remain below 1 for the majority of the cells (Siemens Digital Industries Software, 2025). Also, in terms of cell quality none of the meshes reaches a skewness angle above 80 degrees.

Furthermore, a surface remesher with the *Enhanced quality triangle* option enabled was utilized to make the triangulation of the input geometries more appropriate/optimized for the polyhedral mesh generation.

For each turbulence model and both the heat exchangers, a mesh sensitivity analysis was performed. The mesh sizes of the finned geometry ranged from around 600 000 to 2.5 million cells, meanwhile the tube bundle ranged from around 300 000 to 5 million. The outcomes of the mesh sensitivity analysis can be found in Section 5.1 in the results chapter.

All the specific mesh settings, not kept as default, for each heat exchanger designs can be found in Table 4.4 and 4.5

4.1.4.1 8.0-3/8T single channel mesh

In Table 4.4 below, the specific mesh settings used for the fin & tube geometry can be found.

Table 4.4: The non default mesh settings used for the fin & tube geometry

Mesher	**Surface Remesher**	Meshing method: Enhanced Quality Triangles Curvature refinement ✓ Proximity refinement ✓ Compatibility refinement ✓
	Polyhederal Mesher	
	Prism Layer Mesher	Distribution mode: Wall thickness
Default Controls	**Base Size (604 k cells)** **Base Size (1.3 M cells)** **Base Size (2.5 M cells)**	0.012 m 0.01 m 0.007 m
	Targeted	10% relative to base
	Minimum	0.1% relative to base
	Prism Layer Controls	8 layers Near Wall Thickness: 2.0E-5 m Total Thickness: 4.0E-4 m (Absolute)
	Surface Growth Rate	Slow
	Volume Growth Rate	1.1
	Post Mesh Optimization	✓ ✓
Custom Controls	**Prism Layers**	Disabled on periodic air surfaces and inside solid fin domain
	For the fin domain	Minimum: 4% relative to base Surface Growth Rate: Fast
	For fin trailing and leading edge surface	Target: 1.2% relative to base

4.1.4.2 S 1.50-1.25 single channel mesh

In Table 4.5 below, the specific mesh settings used for the tube bundle geometry can be found.

Table 4.5: The non default mesh settings used for the tube bundle geometry

Mesher	**Surface Remesher**	Meshing method: Enhanced Quality Triangles Curvature refinement ✓ Proximity refinement ✓ Compatibility refinement ✓
	Polyhederal Mesher	
	Prism Layer Mesher	Distribution mode: Wall thickness
Default Controls	**Base Size** **Base Size (4.8 M cells)**	0.01 m 0.0045 m
	Targeted (352 k cells) **Targeted (773 k cells)** **Targeted (1.5 M cells)** **Targeted (3.1 M cells)** **Targeted (4.8 M cells)**	6% relative to base 2% relative to base 1.5% relative to base 1.1% relative to base 2 % relative to base
	Minimum **Minimum (352 k cells)**	0.5% relative to base 2 % relative to base
	Surface Curvature	✓ # Pts/circle: 100
	Prism Layer Controls	8 layers Near Wall Thickness: 2.26E-5 m Total Thickness: 3.733E-4 m (Absolute)
	Surface Growth Rate	Fast
	Volume Growth Rate	1.0
	Post Mesh Optimization	✓ ✓
Custom Controls	**Prism Layers**	Disabled on periodic surfaces

4.1.4.3 8.0-3/8T Unit cell mesh

The mesh settings used for the unit cell domain is kept the same as that of the mesh used for the single channel. The smaller domain size results in a much smaller mesh size of 193 000 cells, a reduction of about 85%.

4.2 Calculations

The calculations presented below are implemented in the simulation model using *parameters* for constant values, together with *reports* for variable flow properties. Flow properties such as temperature, density and total pressure are obtained using

mass flow average or *surface average* reports on the inlet and outlet surfaces, see Figure 4.6.

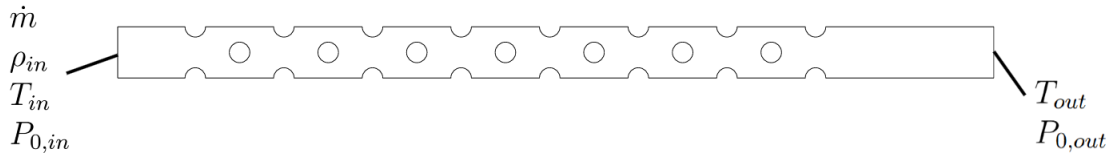

Figure 4.6: The main flow properties that are monitored and used for calculations.

4.2.1 Reynolds Number

The Reynolds number is defined as in *Compact Heat Exchangers*, using the mass velocity G

$$Re = \frac{GD_h}{\mu} \tag{4.1}$$

where G is defined as the mass flow divided by the minimum free-flow area

$$G = \frac{\dot{m}}{A_c} \tag{4.2}$$

Using the mass velocity to define the Reynolds number is more convenient and unambiguous when dealing with flows where temperature, and thus density, is varying, since it stays constant throughout the entire domain.

The hydraulic diameter is defined as

$$D_h = 4L\frac{A_c}{A} \tag{4.3}$$

where A_c is the minimum free-flow area mentioned earlier, A is the total heat transfer area (total wetted area by air), and L is the length of the heat exchanger in the flow direction. These values and how they are derived is presented for both heat exchangers in Tables 4.1 and 4.2.

4.2.2 Friction Factor

In *Compact Heat Exchangers*, Kays & London present an equation for calculating the pressure drop over a heat exchanger (Kays & London, 1984, p.36)

$$\frac{\Delta P}{P_1} = \frac{G^2}{2}\frac{v_1}{P_1}\left[(K_c + 1 - \sigma^2) + 2(\frac{v_2}{v_1} - 1) + f\frac{A}{A_c}\frac{v_m}{v_1} - (1 - \sigma^2 - K_e)\frac{v_2}{v_1}\right] \tag{4.4}$$

The first term within the brackets describes the entrance effects, the second describes flow acceleration, the third describes the core friction and the fourth describes the

exit effects. For flow normal to tube banks, the entrance and exit effect are accounted for in the friction factor, giving $K_e = 0$ and $K_c = 0$. Because the total pressure drop is measured in simulations, the term for the static pressure loss caused by acceleration of the flow can also be ignored. This results in the simplified equation

$$\frac{\Delta P_0}{P_1} = \frac{G^2}{2}\frac{v_1}{P_1}(f\frac{A}{A_c}\frac{v_m}{v_1}) \tag{4.5}$$

Multiplying both sides with P_1 and knowing $v = \frac{1}{\rho}$ and $\frac{A}{A_c} = \frac{4L}{D_h}$, the equation is simplified to

$$\Delta P_0 = \frac{2G^2 L}{D_h \rho_m} f \tag{4.6}$$

This relation is then be used to calculate the friction factor

$$f = \frac{\Delta P_0 D_h \rho_m}{2G^2 L} \tag{4.7}$$

The mean density ρ_m is derived through the ideal gas law at the mean temperature

$$\rho_m = \frac{287 \cdot 101325}{T_m} \tag{4.8}$$

with the mean temperature T_m defined as the mean of T_{in} and T_{out}

The pressure drop ΔP_0 is defined as the difference between the total pressure upstream and downstream of the heat exchanger.

4.2.3 Heat Transfer and Colburn j-factor

The heat transfer coefficient h, based on the formulation in Lotfi and Sunden, 2023, is defined as

$$h = \frac{Q}{A\Delta T_{lm}} \tag{4.9}$$

where Q is the heat transfer

$$Q = \dot{m} c_p (T_{in} - T_{out}) \tag{4.10}$$

and ΔT_{lm} is the logarithmic mean temperature difference

$$\Delta T_{lm} = \frac{(T_{in} - T_w) - (T_{out} - T_w)}{ln(\frac{T_{in} - T_w}{T_{out} - T_w})} \tag{4.11}$$

T_w is the constant wall temperature, in this case the temperature of the tube surfaces.

The heat transfer coefficient together with the mass velocity and fluid properties allows the Colburn j-factor to be obtained through Eq. 2.38.

It is important to note two things before moving on. The first is that, since the

wall temperature on the tubes are constant the overall heat transfer coefficient reduces to the air-side heat transfer coefficient (h) in Eq. 4.9. The second thing is only relevant for the geometry including the fin, and that is the fact that the overall surface efficiency is omitted in Eq. 4.9. This means that the heat transfer coefficient, and thus the Colburn factor, for that geometry, calculated by that equation, corresponds to the "effective" values. This, since the measured resulting temperature difference obtained in the simulation, implicitly, would include any geometry/surface related efficiency. To make the heat transfer coefficient "ideal", Eq. 4.9 would have to be divided by the overall surface efficiency (more on this in the next section).

4.2.4 Fin Efficiency and Overall Surface Efficiency

For the finned geometry, the fin efficiency is derived through the following equation

$$\eta_f = \frac{tanh(m \cdot L_f)}{m \cdot L_f} \tag{4.12}$$

where m is the fin parameter.

$$m = \sqrt{\frac{2h}{k \cdot t_f}} \tag{4.13}$$

The heat transfer coefficient h corresponds to the effective heat transfer coefficient mentioned in the previous section, and calculated from Eq. 4.9. The L_f is the effective fin length and has been defined as half the distance between two tubes in the transverse direction.

$$L_f = \frac{p_t - D_t}{2} \tag{4.14}$$

With the fin efficiency known, the overall surface efficiency of the heat exchanger can be derived through

$$\eta_o = 1 - \frac{A_f}{A}(1 - \eta_f) \tag{4.15}$$

where A_f is the fin heat transfer area. This makes it possible to derive the ideal heat transfer coefficient for the finned geometry via

$$h_{ideal} = \frac{h}{\eta_o} \tag{4.16}$$

This can then be used in Eq. 2.38 to obtain the ideal Colburn factor. Note that, for the tube bundle geometry, these calculations would be irrelevant since it would have an $\eta_o = 1$, and thus have $h_{ideal} = h$.

5

Results and Discussion

5.1 Mesh Sensitivity

The results of the mesh sensitivity analysis are presented in Table 5.1 for the fin & tube geometry, and in Table 5.2 for the tube bundle. For the fin & tube geometry, the sensitivity test was carried out at a fixed Reynolds number of ~ 4300, and for the tube bundle, a Reynolds number of ~ 5747. The *error* column in the tables are the relative error from the finest mesh values of each sweep.

Starting by looking at the sensitivity study for the finned geometry, it can be noted that the relative difference (error-column) is generally low between the 2.5 million size mesh and the 1.3 million size mesh. A change lower than one percent is barely visible in the later f and j result plots so the mesh of around 1.3 million cells was deemed sufficient enough for this geometry. It is however worth to note that some of the turbulence cases doesn't seem to show a completely monotonic convergence. For example, it can be seen that the Realizable k-epsilon jumps between overshooting and undershooting the finest mesh value throughout its range. The variations is on the other hand very small and doesn't change significantly when put into perspective of the later results and therefore deemed negligible. The largest difference between the 1.3 million and the 2.5 million mesh seems to occur for the plain SST k-omega model and the EB k-epsilon model.

Moving on to Table 5.2 for the tube bundle geometry, there are some similarities to the fin & tube. First of all the turbulence configuration least sensitive to mesh refinement is the SST k-omega with Gamma-ReTheta. A similar non monotonic behaviour can also be noted for the Realizable k-epsilon but, like for the fin-tube, the magnitude of the f and j error is pretty much negligible throughout the sweep (Realizable j actually converges monotonically). The least converged cases are the plain SST k-omega and especially the EB k-epsilon. The EB k-epsilon is the turbulence model case where the largest change in result could still be visible. It was concluded that a mesh size of around 3 million cells was to be used for that one. Even though mesh convergence isn't reached, the remaining change is deemed small enough to not alter the conclusions in the later results of this thesis. As for the other models a mesh size of 772 000 cells was chosen.

The selection of mesh sizes is made to balance simulation computational time with mesh convergence. When moving on to the results of this thesis, it can however

be good to have in mind that complete mesh independence is not achieved for all turbulence models. But variations are still deemed small enough to not alter the conclusions of the thesis.

Table 5.1: Mesh convergence results for the 8.0-3/8T single channel

FIN - TUBE

	SST k-omega, Gamma-ReTheta				**SST k-omega**			
Cells	**f**	**Error**	**j**	**Error**	**f**	**Error**	**j**	**Error**
1 259 487	0.0206	-0.82%	0.00465	-0.45%	0.02043	-0.54%	0.004785	0.94%
2 516 816	0.02077	0%	0.00467	0%	0.02054	0%	0.00474	0
	Realizable k-epsilon				**EB k-epsilon**			
	f	**Error**	**j**	**Error**	**f**	**Error**	**j**	**Error**
604 080	0.0191466	0.097%	0.00494	0.61%	0.02073	-1.29%	0.004768	-2.1%
1 259 487	0.018983	-0.76%	0.0049	-0.2%	0.021095	0.45%	0.004828	0.86%
2 516 816	0.019128	0%	0.00491	0%	0.021	0%	0.00487	0%

Table 5.2: Mesh convergence results for the S 1.50-1.25 single channel

TUBE BUNDLE

	SST k-omega, Gamma–ReTheta				**SST k-omega**			
Cells	**f**	**Error**	**j**	**Error**	**f**	**Error**	**j**	**Error**
359037	0.0635	0.78%	0.010467	0.84%	0.05881	1.6%	0.009603	2.5%
772656	0.0631	0.14%	0.010415	0.34%	0.05759	0.68%	0.009491	1.3%
1511404	0.06301	0.0%	0.01038	0.0%	0.0572	0.0%	0.009365	0.0%
3075981								
4834385								
	Realizable k-epsilon				**EB k-epsilon**			
	f	**Error**	**j**	**Error**	**f**	**Error**	**j**	**Error**
359037	0.08278	-0.008%	0.0098719	0.22%	0.06735	6.3%	0.012296	6.4%
772656	0.08254	-0.3%	0.009865	0.15%	0.06618	4.5%	0.01212	4.9%
1511404	0.082587	-0.24%	0.0098564	0.06%	0.06522	3%	0.011926	3.2%
3075981	0.082787	0.0%	0.00985	0.0%	0.06416	1.2%	0.01169	1.2%
4834385					0.06335	0.0%	0.0115563	0.0%

5.2 Validation of f and j_H to Experimental Values

In this section, plots of friction factor and Colburn j-factor values from simulations together with the respective experimental values are presented and discussed. The shaded areas surrounding the fitted lines of experimental data correspond to an uncertainty of ± 5%, which is the estimated uncertainty for the experimental values of both the friction factor and j-factor (Kays & London, 1984, p.152). An uncertainty of ± 2% was estimated for the Reynolds number as well, however this has not been taken into account in the plots.

5.2.1 The 8.0-3/8T single channel

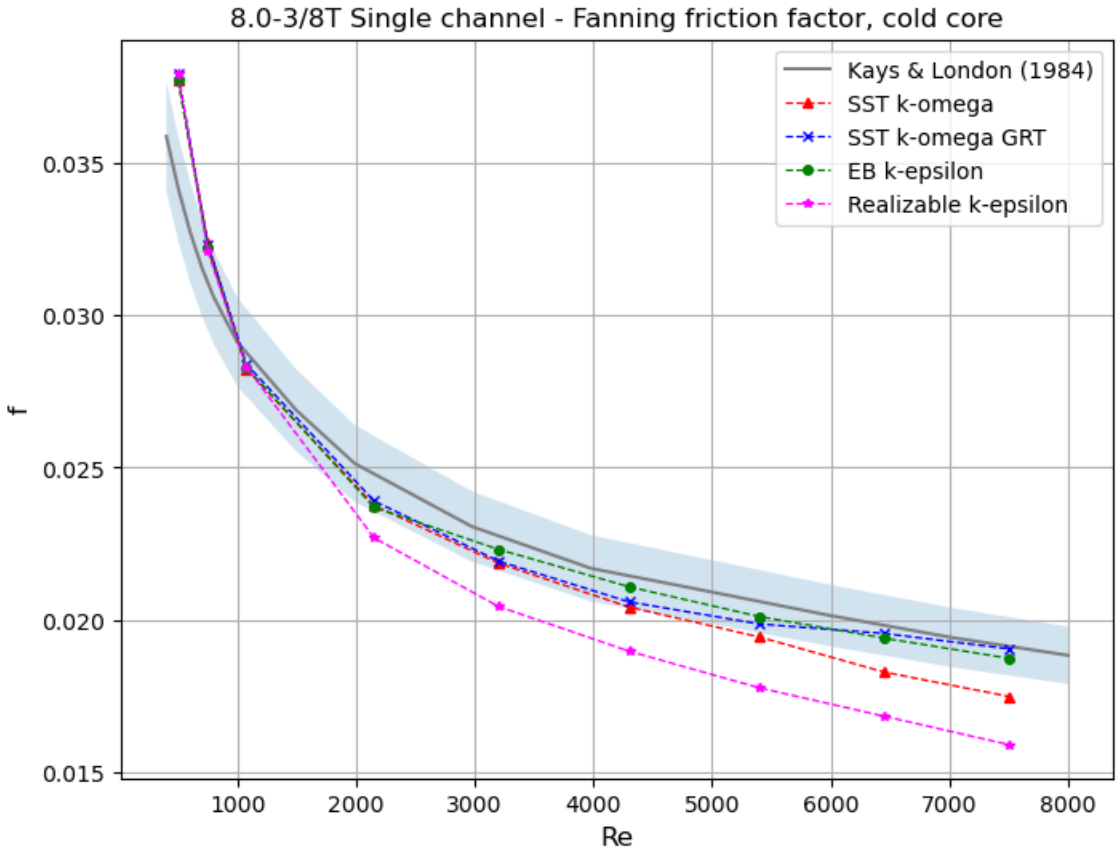

Figure 5.1: Friction factor values plotted against experimental values, 8.0-3/8T single channel

Figure 5.1 shows that two turbulence models achieve consistent values within 5% margin of experimental values for the friction factor; SST k-omega with a Gamma-ReTheta transition model, and the EB k-epsilon model. At lower Reynolds numbers (Re $\lesssim$ 2000), all turbulence models produce very similar f values to each other. At very low Reynolds numbers (Re $\lesssim$ 750) all turbulence models over-predict flow friction. Differences in results between the models start at Re=2000 and increase as

the Reynolds number increases, especially with the SST k-omega and k-epsilon models. SST k-omega without a transition model starts to under-predict slightly after Re=4300, while k-epsilon shows a larger under-prediction already after Re=2100. Another notable thing is that SST k-omega with Gamma-ReTheta starts to level off towards the end of the range, while EB k-epsilon follows the trend better.

In Figure 5.2 the skin friction around the first tube is plotted for each turbulence model at Re=7500, where the friction factor differs the most between the models. The 180 degree point corresponds to the stagnation point at the leading edge of the tube. The skin friction plot shows that the Realizable k-epsilon model produces a boundary layer with higher momentum/energy, as can be seen from the higher peak skin friction coefficient. The higher energy boundary layer is the cause of the more delayed separation point, which in turn results in a smaller wake and thus lower pressure drag for each tube. This is most likely the underlying reason why the Realizable k-epsilon model under-predicts the friction factor.

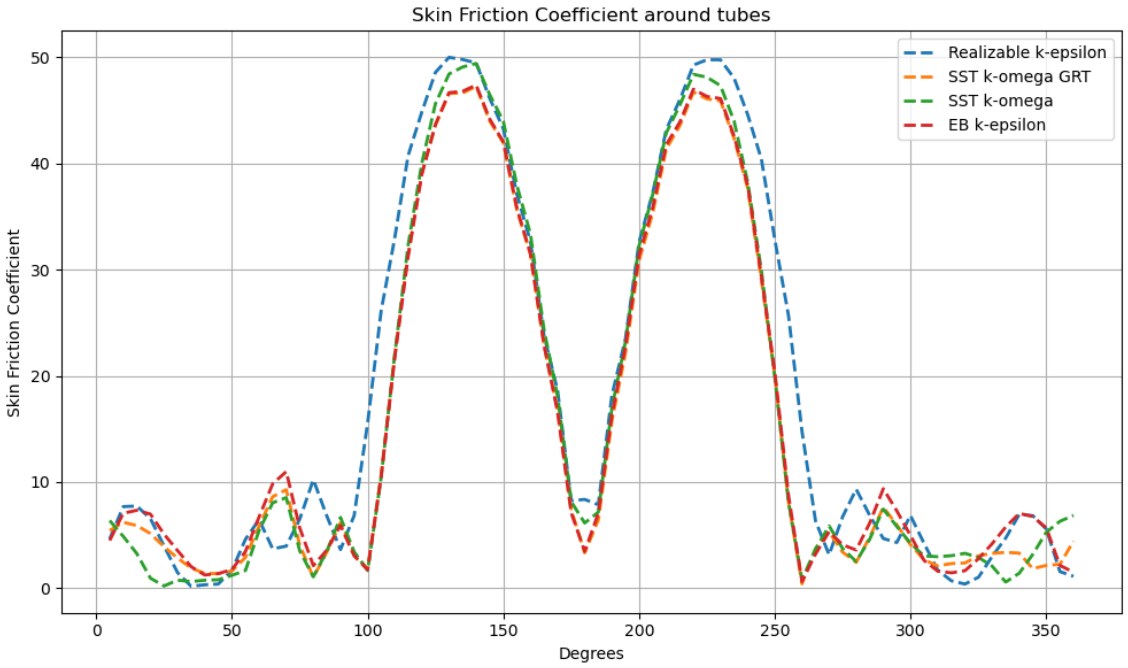

Figure 5.2: Skin friction coefficient around tube, 8.0-3/8T. Re=7500.

Figure 5.3 shows the Colburn j-factor results of the 8.0-3/8T single channel for all turbulence models. While the simulation results capture the general trend quite well, there is a consistent error of 23-28% to experimental values. The differences in results between different turbulence models is quite small however.

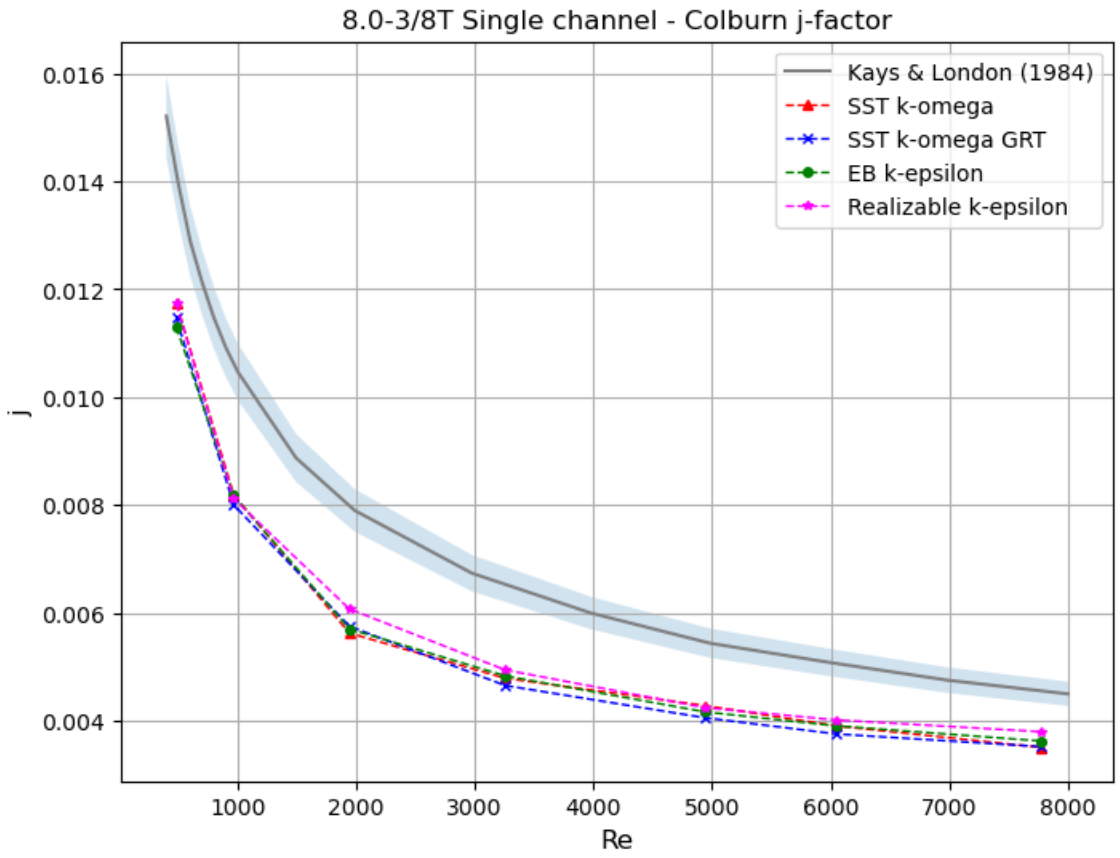

Figure 5.3: Colburn j-factor results plotted against experimental values, 8.0-3/8T single channel.

What could be the source(s) of the larger errors in j-factor values for the fin-tube heat exchanger? One reason could be that computer modelled fins are not perfectly equivalent to the fins on the real physical heat exchanger used in experiments. While a computer modelled fin always has a perfect and consistent thickness, pitch, and interface to the tubes, the same can not always be said for a physical one. Another possibility is that the volume mesh inside the fin is not fine enough. The fin has 2-3 cells along its ”thickness”, but more might be needed to accurately model the conduction throughout the fin. The fin surfaces are modelled as being perfectly smooth as well. On a physical heat exchanger this will not be the case, and a surface roughness might impact the thermal boundary layer and increase heat transfer for the fin. The option to model surface roughness on wall surfaces exists in Star-CCM+ so this could be a thing to look at in future work.

It should be noted that the plot in Figure 5.3 show the *effective* heat transfer values. In other words, without an overall surface efficiency applied to the heat transfer coefficient in Eq. 4.9. Although not clear, it is possible that the experimental data show ideal and not effective values. Figure 5.4 compares effective (no overall efficiency applied) to ideal (overall efficiency applied) values for the Realizable k-epsilon turbulence model. The overall efficiency is derived from the fin efficiency through Eq. 4.15. Fin efficiency results are presented in section 5.5.

What can be seen is that there is a slight increase in Colburn j-factor values, however it does not completely make up for the unusually large error to experimental data.

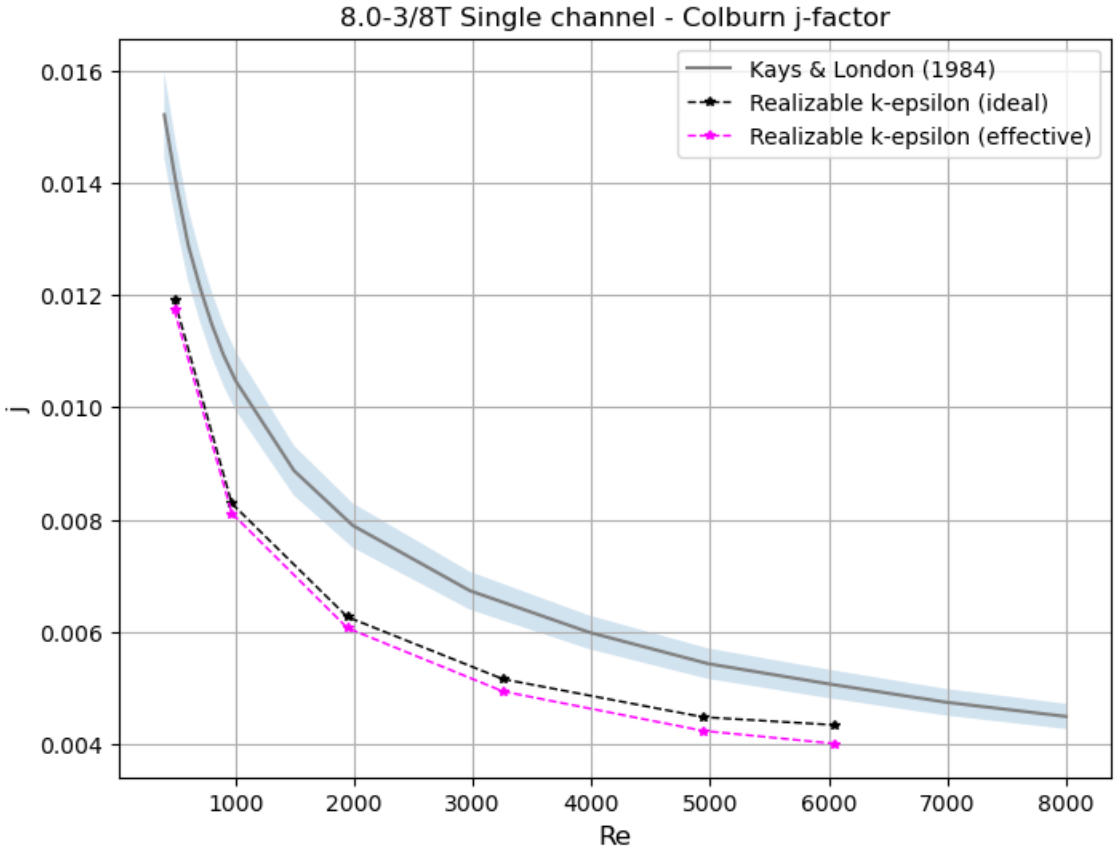

Figure 5.4: Colburn j-factor, effective vs. ideal values, 8.0-3/8T.

5.2.2 The S 1.50-1.25 single channel

In Figure 5.5 the cold core Fanning friction results from the different turbulence models of the tube bundle is plotted over the benchmark (gray line) Reynolds range. The first noticeable thing is how much the different cases vary. The Realizable model (pink line) largely over-predicts the friction factor over the whole range. The plain SST k-omega model (red line) has a hard time following the trend of the benchmark, starts of largely under-predicting the friction in the lower Reynolds region, eventually intersects the benchmark at around $Re = 10\ 000$, and starts to over-predict. It is also worth to note that the smallest Reynolds ($\sim Re\ 900$) cause the plain SST k-omega to become too unstable to get a result. The EB k-epsilon model (green line), produces decent results. At low Reynolds, however, it diverges from the trend and starts to dip. The same slightly happens at the highest Reynolds. Still the magnitude of the friction values (ignoring the low Reynolds region) remain within $\pm 5\%$ of the benchmark. The best results in terms of matching the benchmark comes from the SST k-omega Gamma-ReTheta model (blue line). It captures the overall trend better than the EB k-epsilon model, even though it slightly starts to reach

the upper limit of the ±5% region at the highest Reynolds point. It also still has the same downwards dip in the low Reynolds region as the EB k-epsilon.

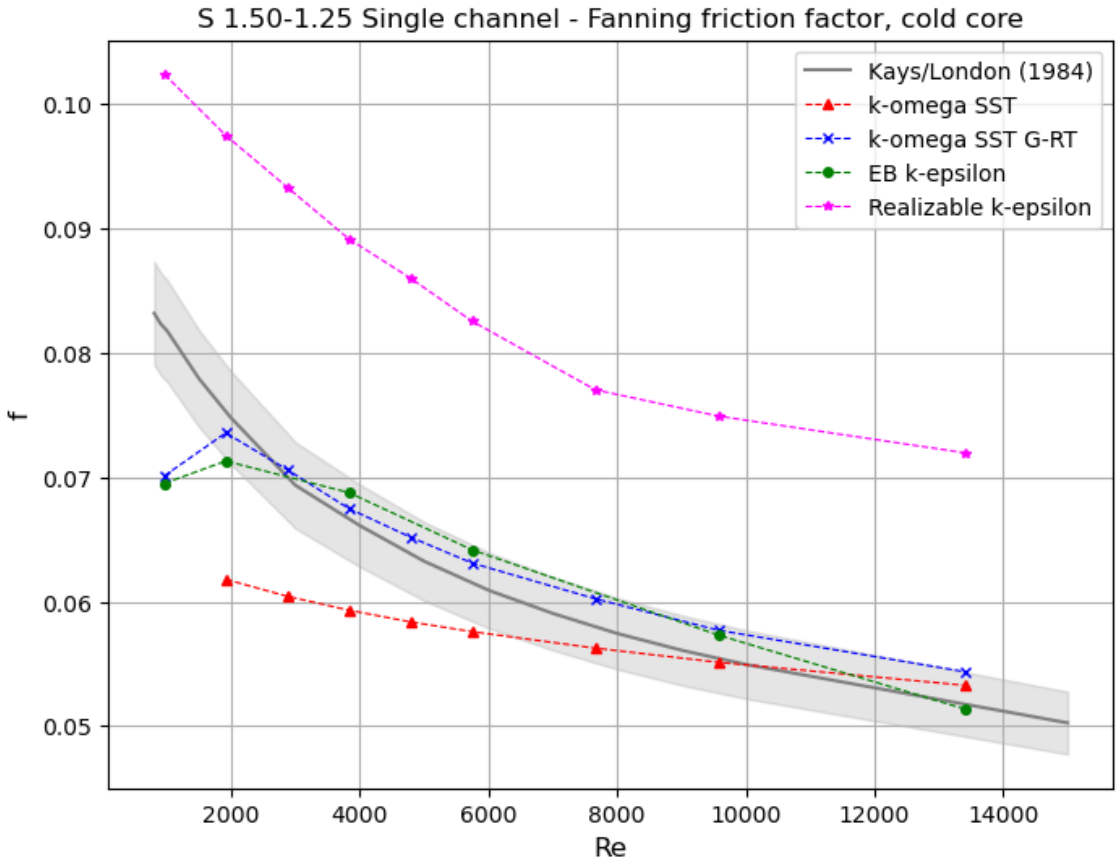

Figure 5.5: Friction factor values plotted against experimental values, S 1.50-1.25 single channel (Cold core)

When it comes to the tube bundle Colburn results (Figure 5.6) the variation between each turbulence model is not as large as with the friction values. Another interesting thing is the fact that the downward dip in the low Reynolds region doesn't appear. All the lines follow the benchmark trend relatively well instead. In the low Reynolds region (Re 900 $-$ Re 2000) the variations between each turbulence model is the smallest. The EB k-epsilon model produces the overall largest over-prediction error from the benchmark with a maximum deviation around $\sim$ 19%. The SST k-omega Gamma-ReTheta model has its largest deviation from the benchmark in the high Reynolds region, deviating around 13%. Its overall deviation from the benchmark is about 10% however. The Realizable k-epsilon over-predicts the most in the low Reynolds region but overall it is slightly closer to the benchmark compared to the SST k-omega Gamma-ReTheta model. The turbulence model producing values closest to the benchmark is the plain SST k-omega model, almost entirely staying within the ±5% shaded area. It does still start to flatten out and increase in deviation at the highest Reynolds point. All in all, none of the turbulence models (except maybe the EB k-epsilon) is drastically deviating from the benchmark. A deviation around ±10% is not an uncommon error when trying to match real experiments with CFD

(Bhuiyan et al., 2015).

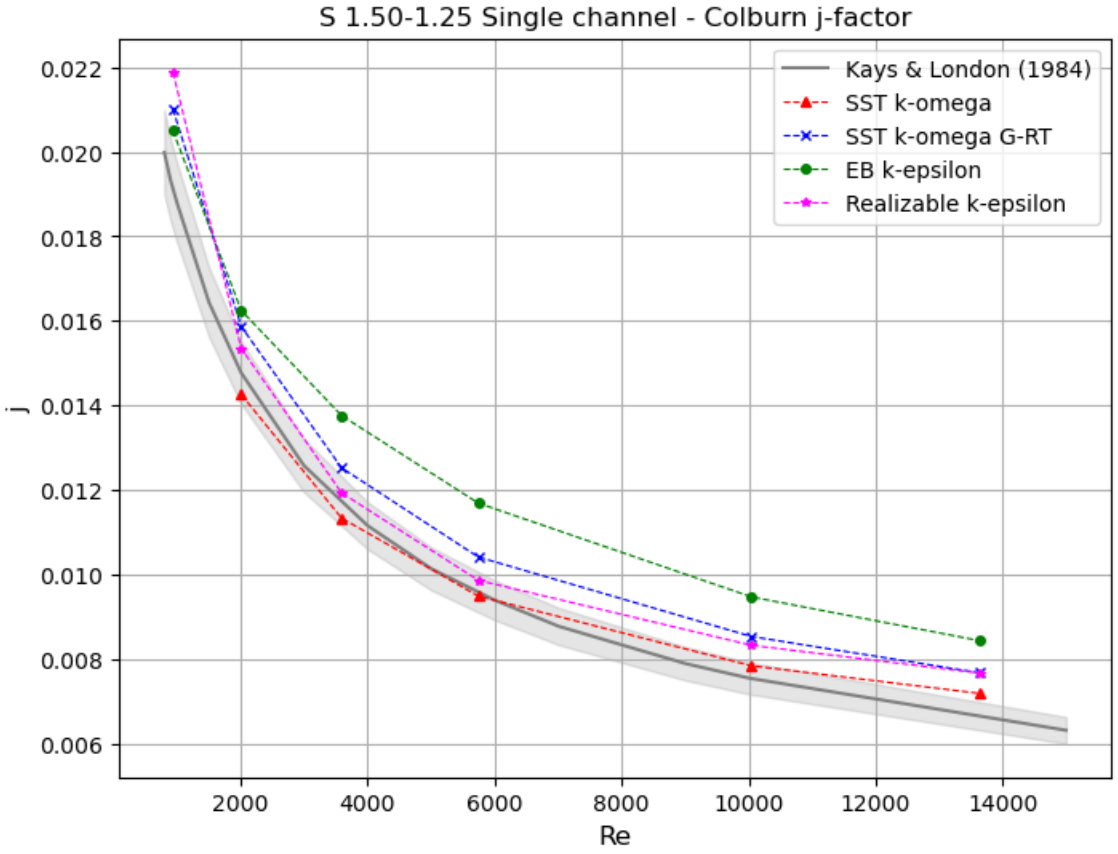

Figure 5.6: Colburn j-factor results plotted against experimental values, S 1.50-1.25 single channel.

The large differences between each turbulence model when it comes to predicting the friction factor shows that numerical modelling of a tube bundle is not trivial. Especially not when it comes to a tightly packed staggered tube configuration. Looking at extracted scenes of total pressure for each turbulence model (Figure 5.7 to 5.10) the correlation between total pressure loss over the channel and the friction factor becomes clear (lower total pressure drop => lower friction factor). Something causes the Realizable k-epsilon model to overestimate total pressure loss, and the addition of a Gamma-ReTheta transition model affect how the SST k-omega model estimates it as well.

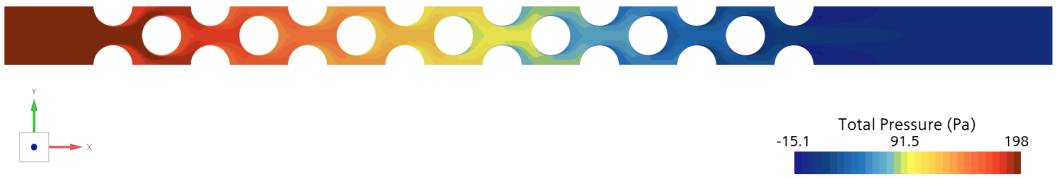

Figure 5.7: Tube bundle total pressure scene at Re=2000, Realizable k-epsilon (relative to gauge)

Figure 5.8: Tube bundle total pressure scene at Re=2000, EB k-epsilon (relative to gauge). Range is in relation the the Realizable range. (Actual range: $[-15 \ \ to \ \ 146 \ Pa]$)

Figure 5.9: Tube bundle total pressure scene at Re=2000, SST k-omega Gamma-ReTheta (relative to gauge). Range is in relation the the Realizable range. (Actual range: $[-15 \ \ to \ \ 146 \ Pa]$)

Figure 5.10: Tube bundle total pressure scene at Re=2000, plain SST k-omega (relative to gauge). Range is in relation the the Realizable range. (Actual range: $[-17 \ \ to \ \ 127 \ Pa]$)

An interesting trend could also be seen when plotting the skin friction coefficient around the tubes. It appears that as the the friction factor gets larger, the flow separates later around the tube circumferences and generates a smaller separation region. This goes against the intuition that an earlier flow separation usually causes a larger separation region and leads to higher pressure drag (as could be seen with the fin-tube geometry). No concrete explanation to exactly why this happens, was able to be determined. But possible correlations to other observations between the two geometries will be made later in Section 5.6 (differences in TKE fields). In Figure 5.11 the skin-friction around a tube in the middle of the domain downstream is plotted for every turbulence model. Note that the stagnation point (i.e. "front" of the tube) is at 180 degrees. To visualize the wake difference, images of the wake around the same middle tube for Realizable k-epsilon and the plain SST k-omega (i.e. the smallest and the largest) are shown in Figure 5.12.

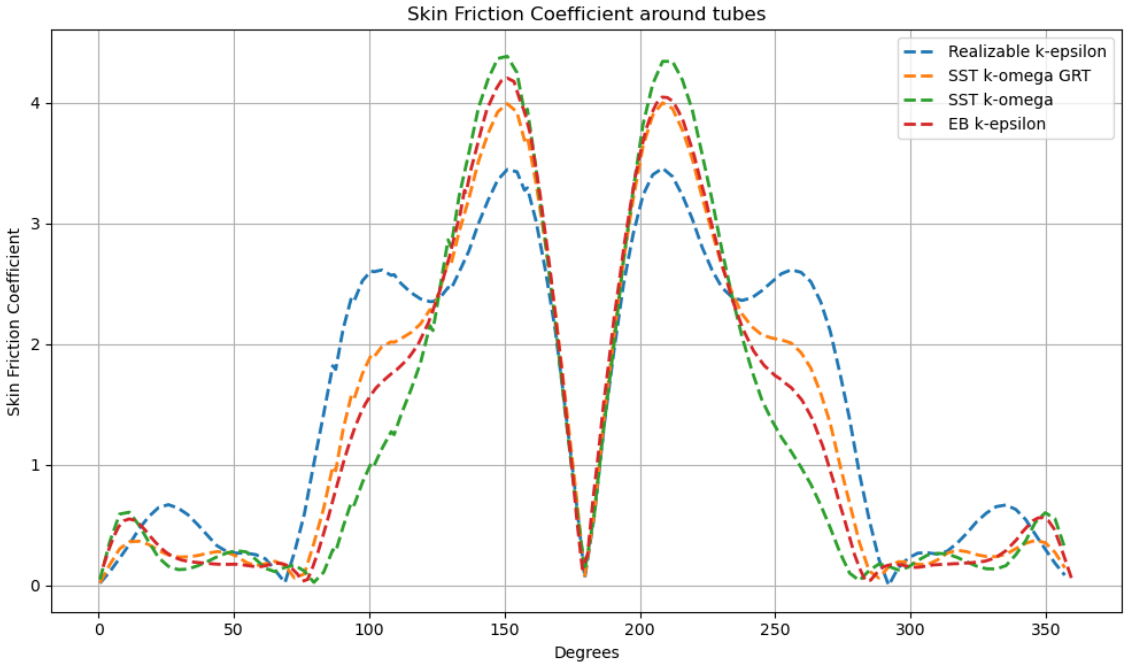

Figure 5.11: Skin friction plots around a tube in the middle downstream of the tube bundle domain

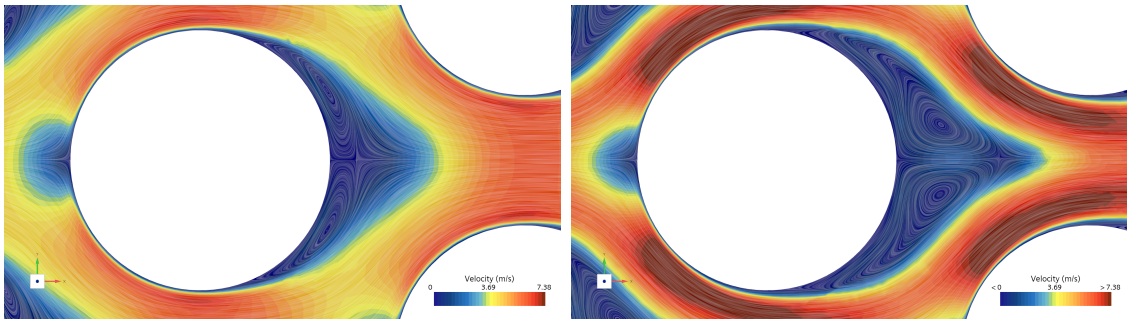

(a) Realizable k-epsilon velocity field **(b)** Plain SST k-omega velocity field

Figure 5.12: Comparison of the wakes after a tube in the middle of the domain downstream, when using the Realizable k-epsilon model (highest friction) and plain SST k-omega model (lowest friction) at Re=2000

This trend together with the total pressure figures suggests that something other than purely wake losses is causing the large variations in the friction coefficient for the tube bundle geometry. Looking at the TKE fields all the turbulence models generate, another interesting trend can be observed. In Figures 5.13 to 5.16 the TKE is visualized over the domain with fixed ranges to the Realizable k-epsilon case to make them comparable.

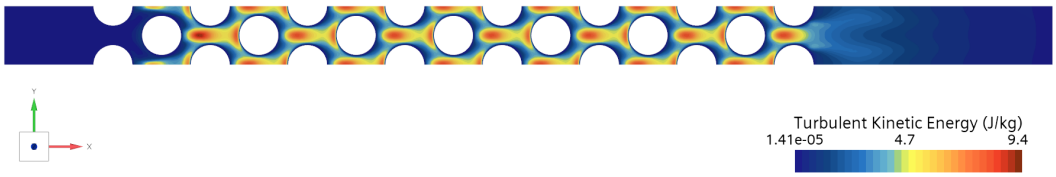

Figure 5.13: Tube bundle TKE scene at Re=2000, Realizable k-epsilon

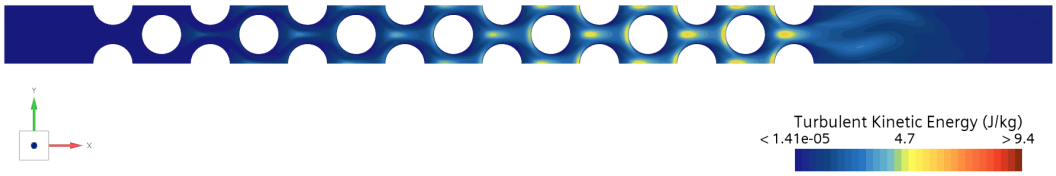

Figure 5.14: Tube bundle TKE scene at Re=2000, EB k-epsilon. Range is in relation the the Realizable range. (Actual range: $[\sim 0 \ \ to \ \ 5.6 \ J/kg]$)

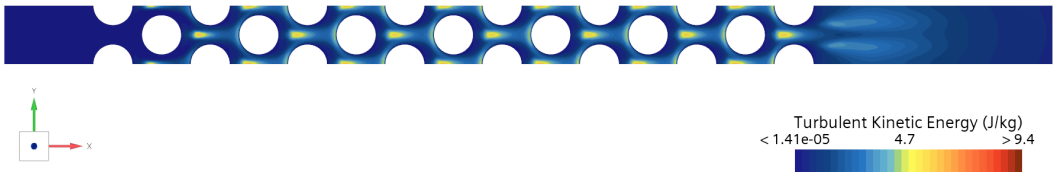

Figure 5.15: Tube bundle TKE scene at Re=2000, SST k-omega Gamma-ReTheta. Range is in relation the the Realizable range. (Actual range: $[\sim 0 \ \ to \ \ 6 \ J/kg]$)

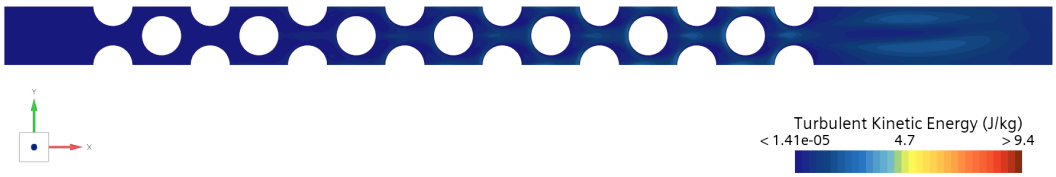

Figure 5.16: Tube bundle TKE scene at Re=2000, plain SST k-omega. Range is in relation the the Realizable range. (Actual range: $[\sim 0 \ \ to \ \ 2.5 \ J/kg]$)

The TKE figures show that the TKE is mainly produced in the narrower acceleration regions between two tubes and in the stagnation region in front of the tubes. The levels of TKE magnitude for each turbulence model also seem to mimic the trend of the friction factor magnitudes (at $Re = 2000$). Realizable k-epsilon has by far the largest maximum magnitude of around 9.4 J/kg, followed by SST k-omega Gamma-ReTheta at around 6 J/kg, EB k-epsilon at around 5.6 J/kg, and lastly the plain SST k-omega with a maximum of only 2.5 J/kg. It is worth mentioning that high acceleration regions and stagnation regions are regions where two-equation eddy viscosity models tend to over-predict TKE production (Vesting, 2024). The implemented turbulence models tackle this in different ways. The Realizable k-epsilon have internal formulations to tackle some of this via the use of damping functions (Siemens Digital Industries Software, 2025; Vesting, 2024). The EB k-epsilon also has its own ”built in” mechanisms (Siemens Digital Industries Software, 2025). For the SST models, the so called *Durbin scale-limiter* is applied. One of the explanations to why the TKE varies so much between the models, and thus the friction factors, could simply be because of the different ways they treat overproduction of TKE in these regions. The fact that the spacing between the tubes in this geometry is very narrow could also be an amplifying factor to this. One thing left to discuss is the fact that both SST k-omega models utilize the *Durbin scale-limiter* but still generates different results. The only thing that varies between the plain SST k-omega and the SST k-omega Gamma-ReTheta set up, is the addition of the transition model. Looking at Figures 5.17 and 5.18 it can be noted that the SST model with transition seem to produce high TKE regions much earlier compared to

the plain SST model. This delay in TKE production could possibly be correlated to why they differ and why the SST k-omega model with Gamma-ReTheta transition generates a larger friction factor closer to the benchmark, compared the plain SST k-omega model. Note that these images aren't with any fixed TKE-range so the colours don't compare to the exact same values.

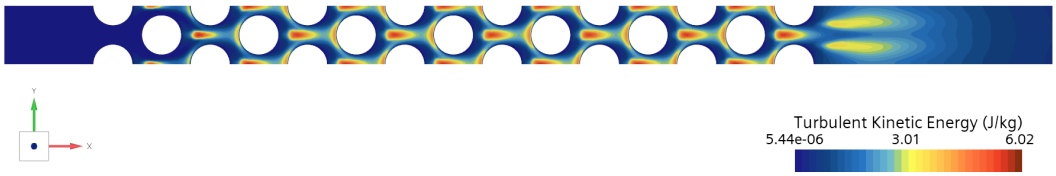

Figure 5.17: Tube bundle TKE scene at Re=2000, SST k-omega Gamma-ReTheta

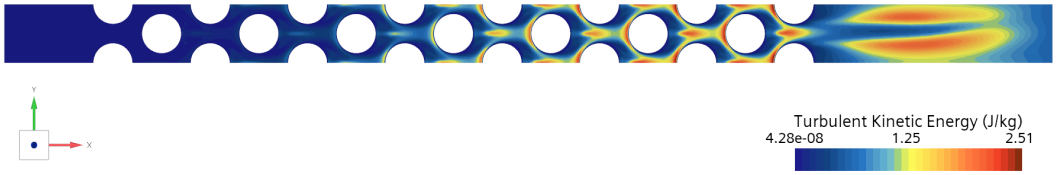

Figure 5.18: Tube bundle TKE scene at Re=2000, plain SST k-omega

5.2.2.1 Turbulence Intensity Analysis of the SST k-omega Gamma-ReTheta model

The Gamma-ReTheta is dependent on free-stream properties such as turbulence intensity (Siemens Digital Industries Software, 2025) and can thus be very sensitive to inlet boundary conditions. Therefore an analysis of a varying turbulence intensity at the inlet-boundary has been performed. The different turbulence intesity values tested have been the standard 5%, then, 10%, 15%, and 20%. A inlet condition value above 5% is usually deemed very high for these kinds of simulations. Those kinds of magnitudes are usually for flow at high-speeds or within complex geometries (CFD Online, 2025). This analysis was mainly done to see how sensitive the Gamma-ReTheta model would be. Figures 5.19 and 5.20 shows the results for the Fanning friction and j-factor results respectively. It can once again be seen that the j-factor doesn't seem to be affected that much since only minimal variations between the lines occur. The only affect it has is in the low Reynolds region where an increase in turbulence intensity lead to an increase in j-factor.

For the friction values, something interesting can be observed however. The low Reynolds dip gradually disappear when increasing the inlet turbulence intensity. It

is also interesting how only the values in the low Reynolds region becomes affected, the values in the rest of the Reynolds range stay more or less unchanged. Since an inlet turbulence intensity above 5% most likely is excessively high, it is possible that arbitrarily increasing it compensate for some other phenomena not able to be captured by the standard set up.

This turbulence sensitivity study does however conclude that the Gamma-ReTheta model is largely sensitive to the inlet turbulence intensity boundary condition.

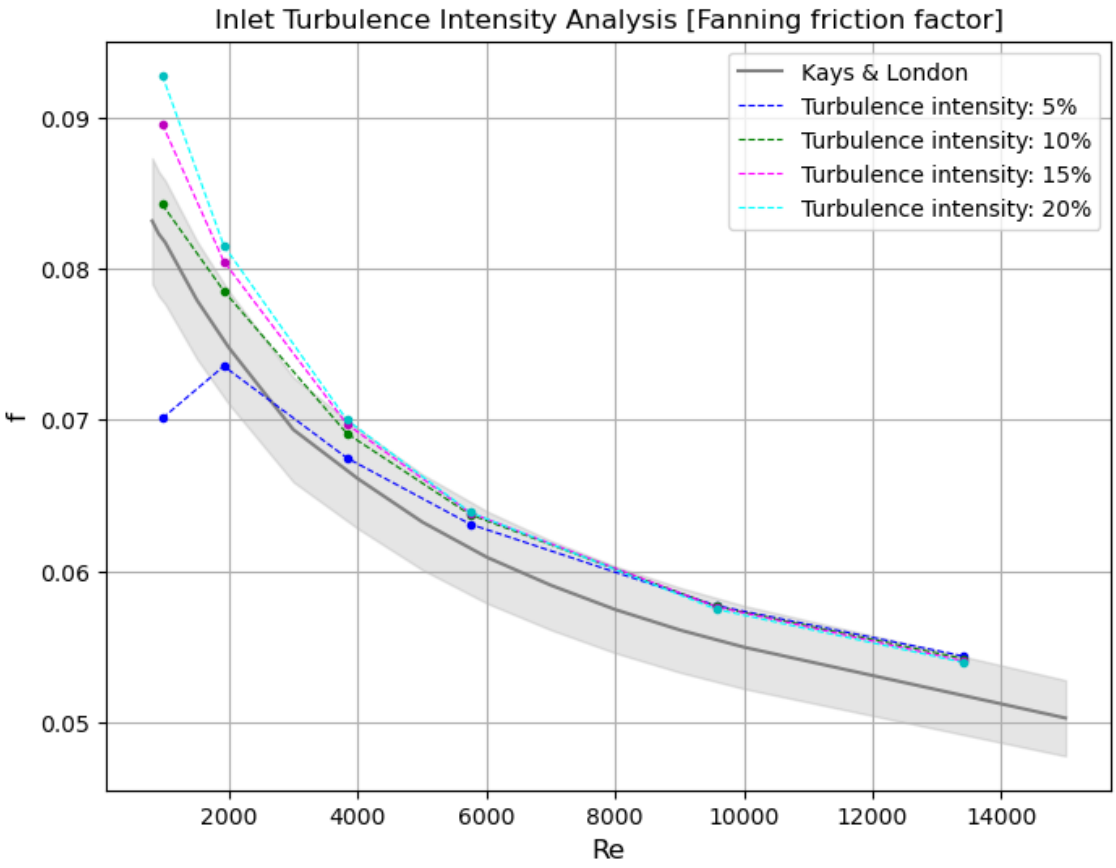

Figure 5.19: Tube bundle, inlet turbulence intensity result of the Fanning friction factor

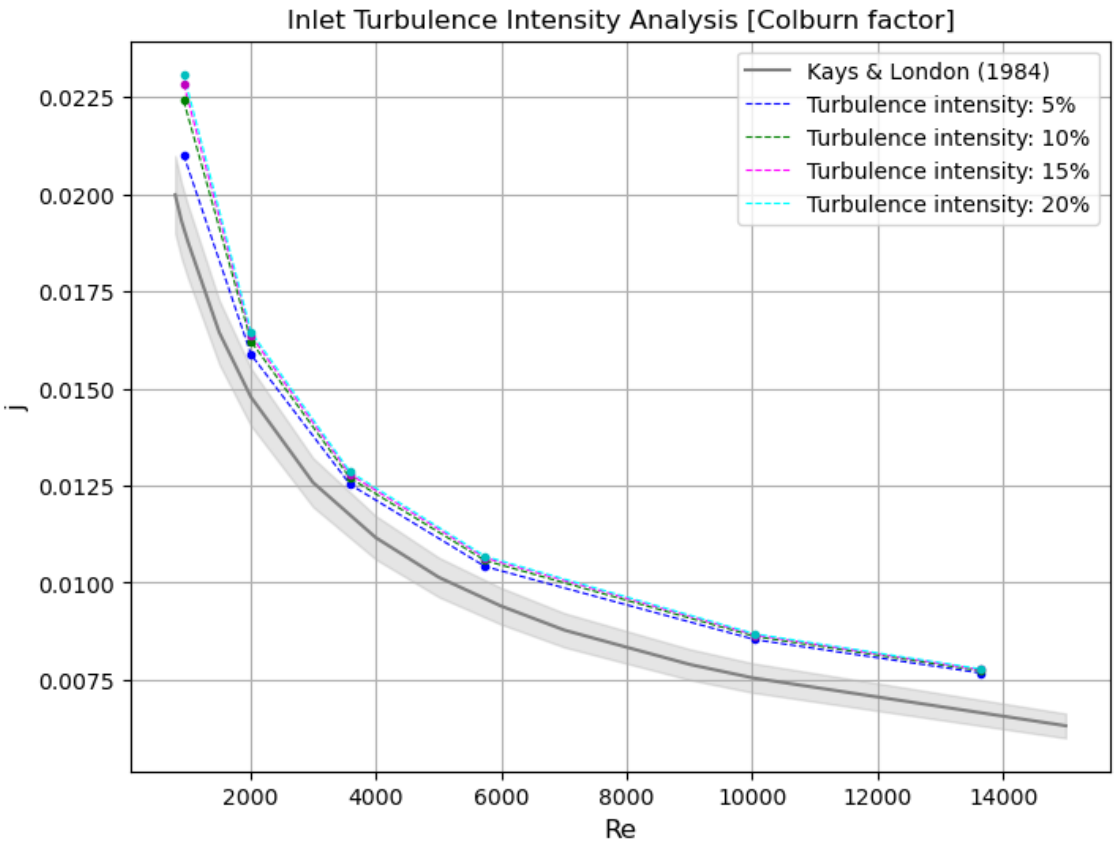

Figure 5.20: Tube bundle, inlet turbulence intensity result of the Colburn factor

5.3 Flow Development

How the flow develops along the tube rows within the single channel domain has been studied by dividing the domain in to 7 separate unit cells and monitoring the pressure drop and heat transfer over each one, see Figure 5.21. A friction factor and j-factor is thus obtained for each unit cell and is plotted.

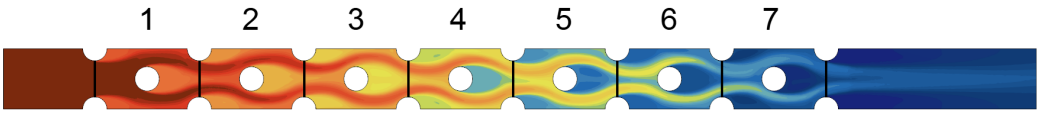

Figure 5.21: The domain is divided in to 7 unit cells to study flow development

At certain Reynolds numbers, there is a clear convergence of friction factor values after around 5 unit cells, see Figure 5.22. The plots also show that the global value, i.e. the friction factor measured for the whole domain, is close to this converged value.

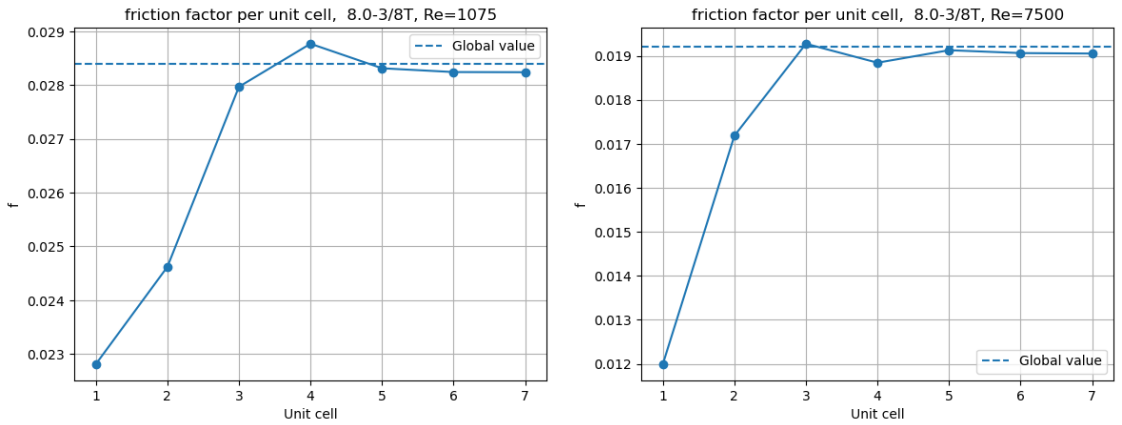

(a) Re=1075 **(b)** Re=7500

Figure 5.22: Friction factor for each unit cell.

Results are not so clear at all Reynolds numbers however. Figure 5.23a shows how the friction factor has not quite converged within the domain. The reason for this could be asymmetric flow and a flow field that is not completely converged. Figure 5.23b shows instead that the friction factor for the whole domain is higher than for each unit cell. The reason for this is most likely that there are further losses in total pressure caused by mixing between the end of the heat exchanger and the domain outlet, where the downstream total pressure is measured.

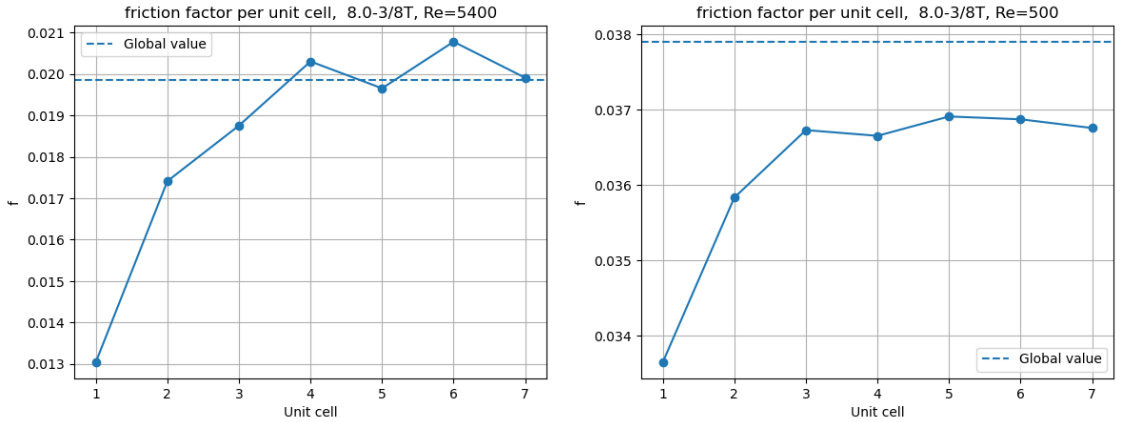

(a) Re=5400 **(b)** Re=500

Figure 5.23: Friction factor for each unit cell.

While all plots may not show completely converged values, there are some clear similarities between all simulations. One takeaway is that there is a steep increase in friction factor between the first, second and third unit cell, meaning that the flow may not yet be fully developed there. As a general rule, one could conclude that the pressure drop will most likely converge after 3-5 unit cells.

Similar results can be seen for the j-factor. Figure 5.24 shows two simulations

were the j-factor values have converged after 5 to 6 unit cells. Again, a sharp drop can be seen between the first, second and third unit cell values.

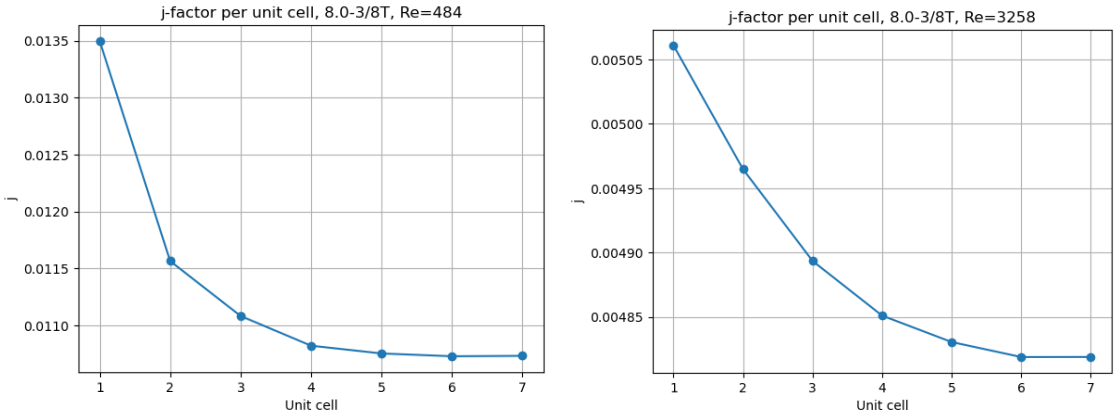

(a) Re=484 **(b)** Re=3258

Figure 5.24: Colburn j-factor for each unit cell.

5.4 Periodic Unit Cell

In this section, results from periodic unit cell simulations are presented along with discussion of the results and methods. All results shown in the plots are from simulations were the flow is controlled through the *pressure jump* option. Figure 5.1 shows the friction factor results using the SST k-omega model with Gamma-ReTheta, compared to the single channel results and experimental values.

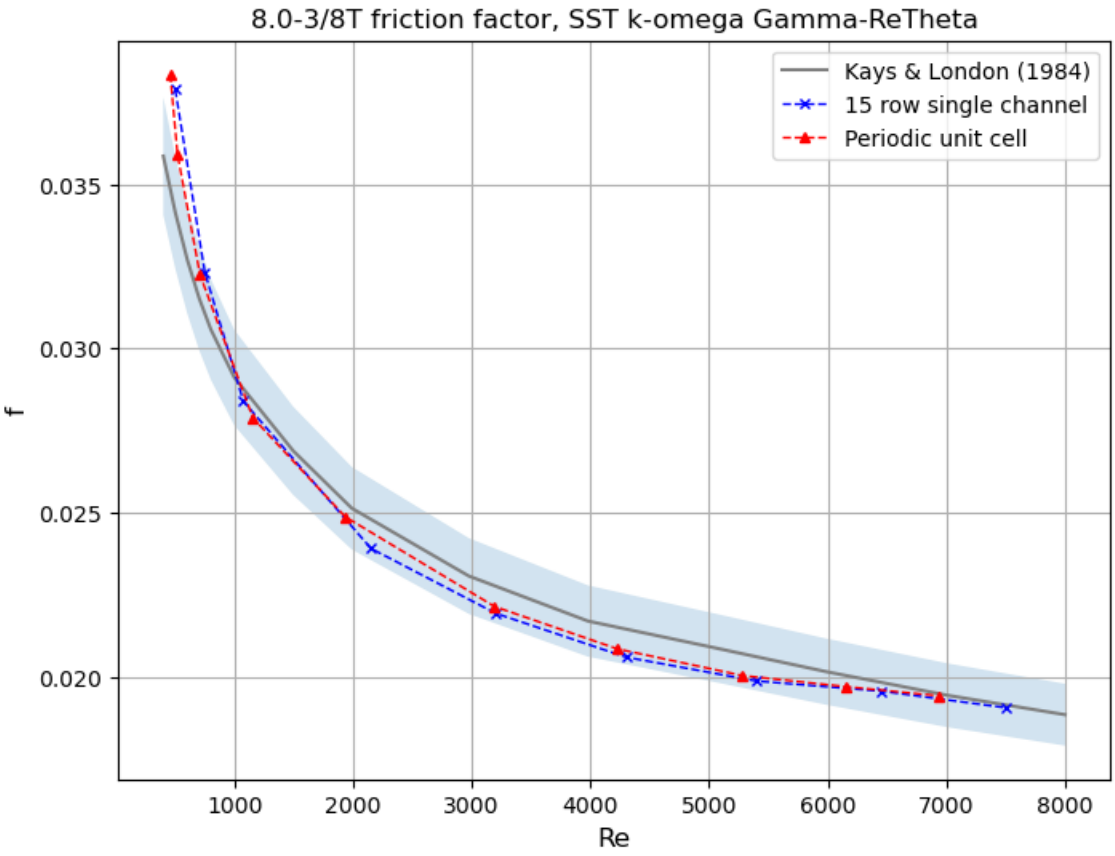

Figure 5.25: Friction factor results for the 8.0-3/8T unit cell

Figure 5.26 shows the Colburn j-factor results compared with the single channel results and experimental values.

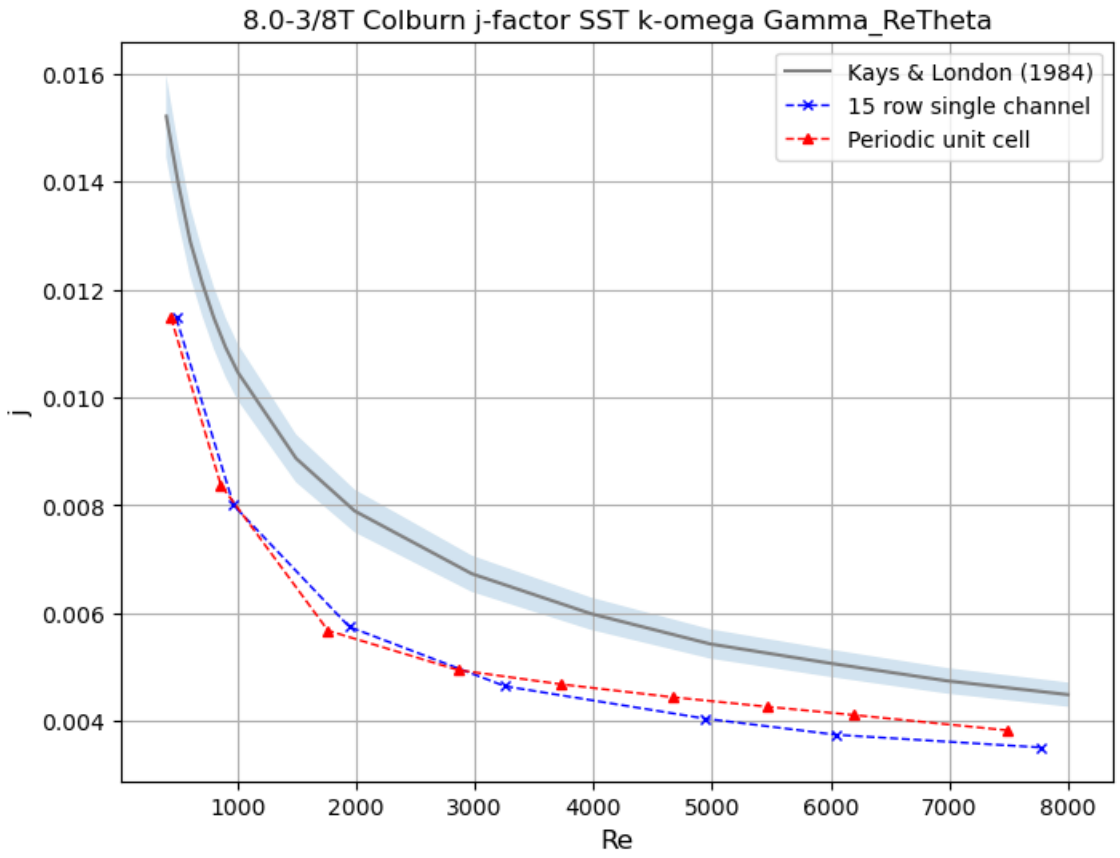

Figure 5.26: Colburn j-factor result for 8-03/8T unit cell

The first thing that can be noted when looking at the results from the unit cell simulations is that they are quite similar to the results from the single channel domain, in both the general trends and absolute values. The conclusions that can be made from this are that 1) The flow in the single channel domain is fully developed and values converged 2) The general simulation setup is robust and produces very similar results with two different domains and approaches. Another notable thing is that the under-prediction of the j-factor remains.

The reason for using the *pressure jump* option to control the flow over the fully developed periodic interface is that the coupled solver struggles to reach a fully developed flow and the desired mass flow rate when using the *target mass flow rate* option. Instead, the flow ”dies”, or stagnates. While the pressure jump is imposed directly when using the *pressure jump* option, the solver instead tries to reach the mass flow across the interface iteratively by adjusting the pressure jump when the *target mass flow rate* option is used. This issue is most likely connected to how the coupled solver solves the momentum and continuity equations simultaneously as a single matrix system. The reasonable response to this problem would be to switch to a segregated solver instead, which solves pressure and velocity iteratively. The segregated solver has its own issues however. While a fully developed flow is quickly reached using a segregated solver with the *target mass flow* option, the flow will eventually distort. Small asymmetries in the flow get fed back in to the domain

through the periodic interface and grow, causing a feedback loop. It is possible that this could be mitigated by lowering or ramping under-relaxation factors, but no successful attempts of this were made. Another method could be to initialize a fully developed flow with the use of a segregated solver, and then switch to a coupled solver to keep the solution stable. The authors leave this to be investigated in future work. The pressure drop being the input variable when simulating a heat exchanger is perhaps not ideal, since it is more likely that a known mass flow or inlet velocity will be used to obtain a pressure drop rather than the other way around. If this is the case, one can start by guessing a pressure drop across the domain, monitor the produced mass flow or velocity, and iteratively adjust the pressure drop until the desired flow is achieved.

5.5 Fin Efficiency

Figure 5.27 shows the fin efficiency of the 8.0-3/8T single channel calculated using Eq. 4.12.

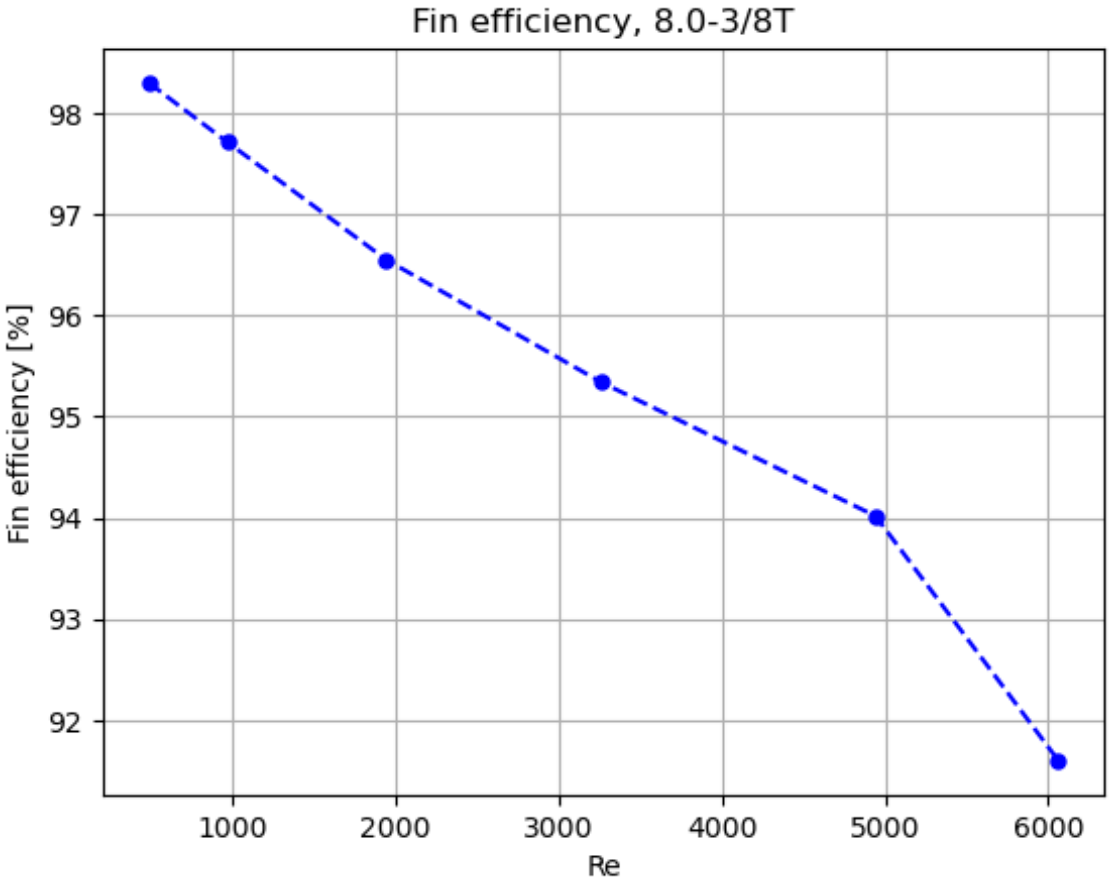

Figure 5.27: Fin efficiency vs. Reynolds number, 8.0-3/8T

The fin efficiency spans from 98.3% at Re=484 to 91.6% at Re=6063. These values are quite reasonable for a compact aluminium fin-tube heat exchanger, especially

considering that it is computer modelled and therefore does not suffer from the effects of fouling, poor tolerances or mechanical damage (Lord Fin Tube, 2025), (United Heat Exchangers, 2026).

The fin efficiency values correlate reasonably to fin temperature contour plots as well. Figure 5.28 shows the fin temperature with the range $280K \leq T \leq 300K$ for Re=484. Almost the entire fin surface area is at 280 K, which is the base temperature. This corresponds to a high fin efficiency. Figure 5.29 shows the same plot at the highest Reynolds number of 6063. A larger part of the surface area is deviating from the base temperature, resulting in a lower fin efficiency.

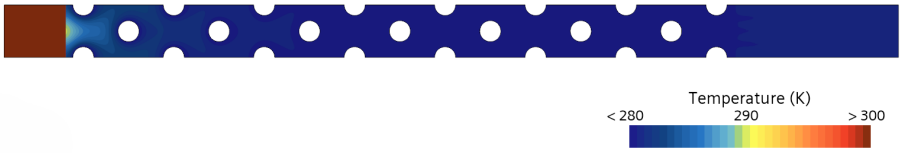

Figure 5.28: Fin temperature, Re=484

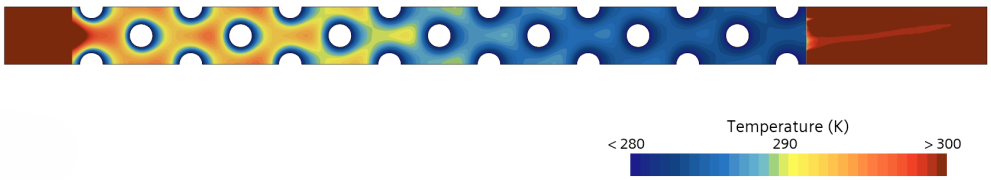

Figure 5.29: Fin temperature, Re=6063

5.6 Discussion on Differences Between Flow In the Fin-Tube and the Tube Bundle Geometry

Comparing the results of the two heat exchanger geometries, there are some differences that can be noted. First of all, the fin-tube geometry seem to show trends of the friction factor correlating to the fact that an earlier separation and a larger wake behind the tubes corresponds to a higher friction value. The exact opposite of this trend is observed for the tube bundle geometry. One hypothesis for why this could be is that it has to do with the fact that the spacing between the tubes in the fin-tube exchanger is substantially larger than that of the tube bundle. Another difference in the results is the magnitude of TKE, especially in the acceleration and stagnation regions between the tubes. In these regions, the TKE of the tube bundle is much larger than that of the fin-tube exchanger who seem to have much more TKE concentrated in the outlet area of the domain, see Figure 5.30. This could be a consequence of the smaller tube spacing in the tube bundle. In other words, that design is much more aggressive on the turbulence models which cause the main pressure loss contributor to switch from mainly wake related losses for the fin-tube,

to pressure losses, more related to momentum dissipation caused by turbulence production and mixing etc. The fin itself is probably another large contributing factor when it comes to the different behaviour of the f and j_H results. In the tube bundle, flow is only governed by cylindrical tube interactions (constantly separating and accelerating the flow). Meanwhile, in the fin-tube geometry the flow is confined within flat plate-like fin channels, having their own thermal and fluid boundary layer.

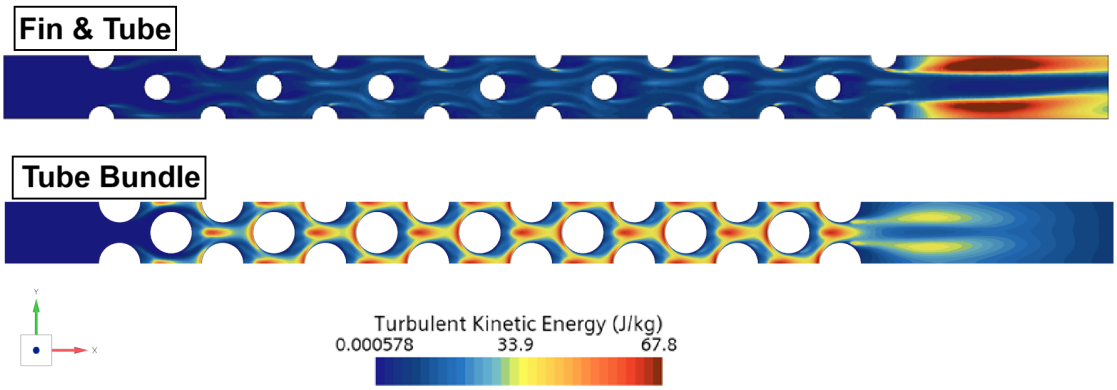

Figure 5.30: Comparison of TKE fields of the fin-tube geometry (above) and tube bundle geometry (below) at Re = 7500 (Note, domains are not at same geometric scale)

6
Conclusions

The following conclusions can be made from this thesis:

- The SST k-omega model with Gamma-ReTheta transition has shown the best general ability to replicate experimental data and capture trends.
- Simulations of tube bundles, especially with compact small tubes, are complex and flow friction solutions are highly sensitive to the simulation setup, especially at low Reynolds flow.
- Choice of turbulence model has a greater impact on flow friction than heat transfer.
- Periodic unit cell simulations are able to produce very similar results to single channel simulations, with greatly reduced cell count.

Bibliography

Altwieb, M., Kubiak, K. J., Aliyu, A. M., & Mishra, R. (2020). A new three-dimensional cfd model for efficiency optimisation of fluid-to-air multi-fin heat exchanger. *Thermal Science and Engineering Progress*, *19*, 100658. https://doi.org/10.1016/j.tsep.2020.100658

Bergman, T. L. (2020). *Fundamentals of heat and mass transfer*. Wiley.

Bhuiyan, A. A., Amin, M., Naser, J., & Islam, A. S. (2015). Effects of geometric parameters for wavy finned-tube heat exchanger in turbulent flow: A cfd modeling. *Frontiers in Heat and Mass Transfer*, *6*. https://doi.org/10.5098/hmt.6.5

Bhuiyan, A. A., Amin, M. R., Karim, R., & Islam, A. S. (2014). Plate fin and tube heat exchanger modeling: Effects of performance parameters for turbulent flow regime. *International Journal of Automotive and Mechanical Engineering*, *9*, 1768–1781. https://doi.org/10.15282/ijame.9.2013.25.0147

Billard, F., & Laurence, D. (2012). A robust kv2¯/k elliptic blending turbulence model applied to near-wall, separated and buoyant flows. *International Journal of Heat and Fluid Flow*, *33*(1), 45–58. https://doi.org/https://doi.org/10.1016/j.ijheatfluidflow.2011.11.003

CFD Online. (2012). Finite volume [CFD-Wiki]. Retrieved May 30, 2026, from https://www.cfd-online.com/Wiki/Finite_volume

CFD Online. (2024, December). *Turbulence length scale* [CFD-Wiki]. Retrieved June 3, 2026, from https://www.cfd-online.com/Wiki/Turbulence_length_scale

CFD Online. (2025, January). *Turbulence intensity* [CFD-Wiki]. Retrieved June 3, 2026, from https://www.cfd-online.com/Wiki/Turbulence_intensity

Chu, W.-X., Sheu, W.-J., Hsu, C.-C., & Wang, C.-C. (2020). Airside performance of sinusoidal wavy fin-and-tube heat exchangers subject to large-diameter tubes with round or oval configuration. *Applied Thermal Engineering*, *164*, 114469. https://doi.org/10.1016/j.applthermaleng.2019.114469

Durbin, P. A. (1993). A reynolds stress model for near-wall turbulence. *Journal of Fluid Mechanics*, *249*, 465–498. https://doi.org/10.1017/S0022112093001259

Johansson, C. (2021, December). *Coupled solver settings in simcenter star-ccm+*. https://volupe.com/simcenter-star-ccm/coupled-solver-settings-in-simcenter-star-ccm/

Kays, W. M., & London, A. L. (1984). *Compact heat exchangers* (3rd ed.). McGraw-Hill.

Li, D. (2019). Turbulent prandtl number in the atmospheric boundary layer: Where are we now? *Atmospheric Research*, *216*, 86–105. https://doi.org/10.1016/j.atmosres.2018.09.015

Lord Fin Tube. (2025, March). *Finned tubes heat transfer efficiency guide*. Retrieved June 7, 2026, from https://www.lordfintube.com/finned-tubes-heat-transfer-efficiency-guide_1720.html

Lotfi, B., & Sunden, B. A. (2023). A novel trussed fin-and-elliptical tube heat exchanger with periodic cellular lattice structures. *International Journal of Numerical Methods for Heat & Fluid Flow*, *33*(3), 1076–1115. https://doi.org/10.1108/HFF-04-2022-0206

Menter, F. R. (1994). Two-equation eddy-viscosity turbulence modeling for engineering applications. *AIAA Journal*, *32*(8), 1598–1605. https://doi.org/10.2514/3.12149

Obiso, D. (2023, June). *Fasten your seat belts: The coupled solver is taking off on gpu!* Siemens Digital Industries Software. Retrieved June 3, 2026, from https://blogs.sw.siemens.com/simcenter/cfd-coupled-solver-is-taking-off-on-gpu/

Siemens Digital Industries Software. (2025). *Simcenter STAR-CCM+ User Guide* (version 2506).

SimScale GmbH. (2023). K-epsilon turbulence models [Last updated: 20 July 2023].

SimScale GmbH. (2025). K-omega turbulence model [Last updated: 8 April 2025].

United Heat Exchangers. (2026, March). *Buy finned tube heat exchangers: Custom & fast delivery*. Retrieved June 7, 2026, from https://www.unitedheatexchangers.com/heat-exchanger/finned-tube-heat-exchanger

Versteeg, H. K., & Malalasekera, W. (2007). *An introduction to computational fluid dynamics: The finite volume method* (2nd ed.). Pearson Education Limited.

Vesting, F. (2024, September). Enhancing turbulence models in simcenter star-ccm+ [Accessed: 2026-06-08].

Volupe. (n.d.). *Y+ calculator*. Retrieved June 24, 2026, from https://volupe.com/support/all-y-calculator-when-meshing-a-geometry-for-cfd-analysis/

Wang, C. C., Chi, K. Y., & Chang, C. J. (2000). Heat transfer and friction characteristics of plain fin-and-tube heat exchangers, part ii: Correlation. *International Journal of Heat and Mass Transfer*, *43*(15), 2693–2700.

Webb, S. W., & Cook, J. T. Les data-model comparisons for flow over a tube bundle including heat transfer. In: In *International heat transfer conference 13*. 2006.

Weiss, J. M., & Smith, W. A. (1995). Preconditioning applied to variable and constant density flows. *AIAA Journal*, *33*(11), 2050–2057. https://doi.org/10.2514/3.12946

White, F. M. (2011). *Fluid mechanics*. Tata Mcgraw Hill Education.

Wilcox, D. C. (1988). Re-assessment of the scale-determining equation for advanced turbulence models. *AIAA Journal*, *26*(11), 1299–1310. https://doi.org/10.2514/3.10041

A

Drawing of 8.0-3/8T Single Channel Domain

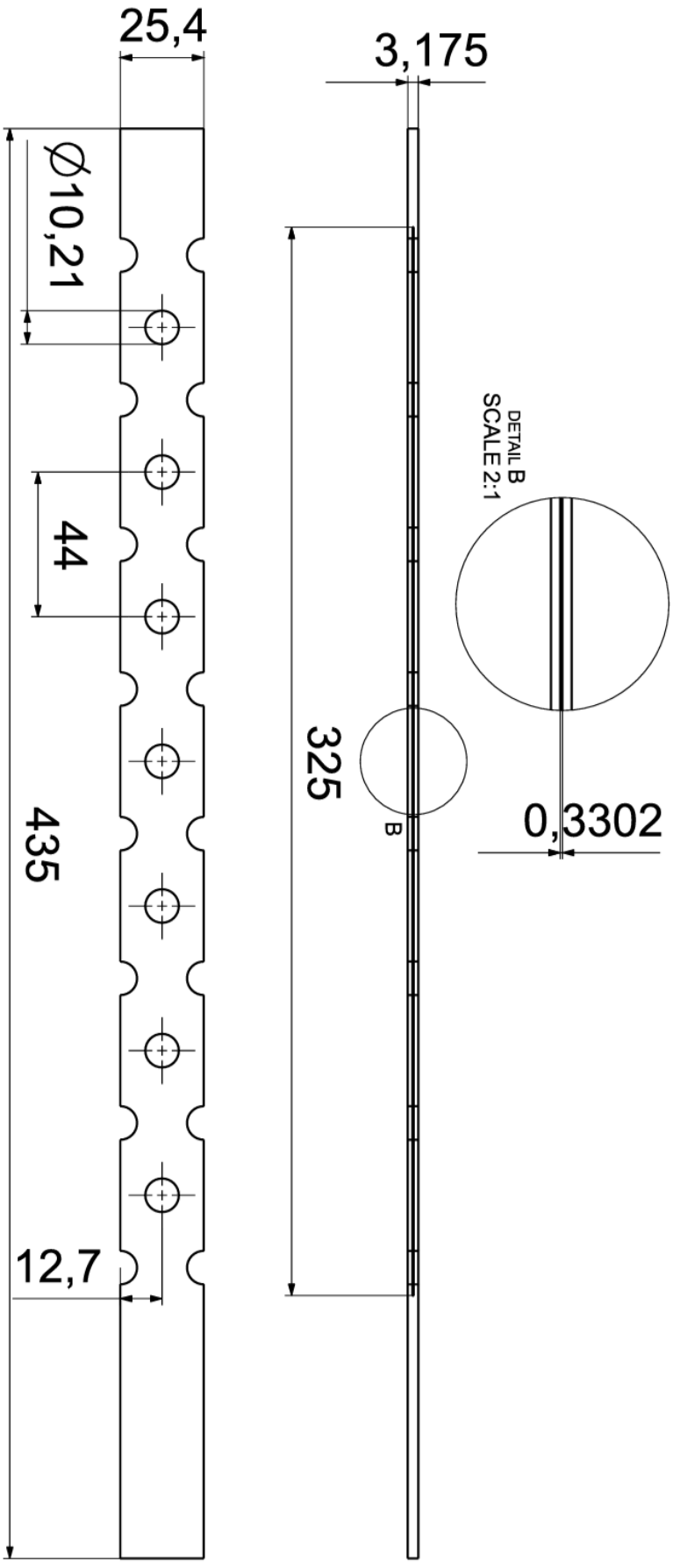
25,4
3,175
Ø10,21
44
435
12,7
325
B
DETAIL B
SCALE 2:1
0,3302

B

Drawing of S 1.50-1.25 Single Channel Domain

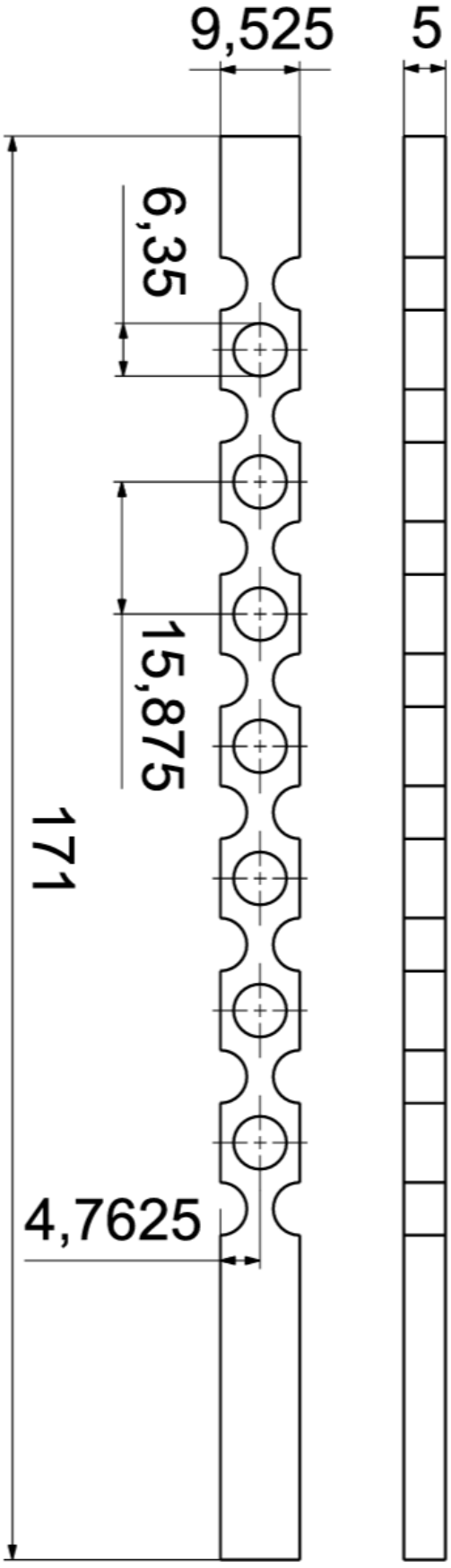
9,525
5
6,35
15,875
171
4,7625

DEPARTMENT OF MECHANICS AND MARITIME SCIENCES
CHALMERS UNIVERSITY OF TECHNOLOGY
Gothenburg, Sweden
www.chalmers.se

CHALMERS
UNIVERSITY OF TECHNOLOGY